International Journal of Solids and Structures 339 (2026) 114190

Contents lists available at ScienceDirect

International Journal of Solids and Structures

journal homepage: www.elsevier.com/locate/ijsolstr

Digital twins for soft pneumatic actuators via reduced-order surrogate modeling

Yichen Pu [a], Xinjie Hu [a], Xingrui Liu [a], Shichao Niu [b], Ning An [a,c,*]

[a] Robotic Satellite Key Laboratory of Sichuan Province, Key Laboratory of Advanced Spatial Mechanism and Intelligent Spacecraft, Ministry of Education, School of Aeronautics and Astronautics, Sichuan University, Chengdu 610065, People's Republic of China

[b] Key Laboratory of Bionic Engineering, Ministry of Education, Jilin University, Changchun 130022, People's Republic of China

[c] Department of Civil, Environmental and Mechanical Engineering, University of Trento, Trento, 38123, Italy

ARTICLE INFO

Dataset link: https://github.com/SCU-An-Group/DT4SoRo

Keywords:
Reduced-order modeling
Digital twin
Pneumatic actuator
Soft robotics

ABSTRACT

Soft pneumatic actuators are widely used in soft robotics because of their compliance and ability to generate smooth, biomimetic motions. However, accurately modeling their highly nonlinear and deformable behavior, particularly under contact conditions, remains computationally intensive, limiting their integration into real-time control and digital twin frameworks. This study presents a reduced-order surrogate modeling approach to enable a real-time-capable digital twin for soft pneumatic bending actuators. High-fidelity simulations based on finite element modeling (FEM) are first used to generate full-field response snapshots, which are reduced using proper orthogonal decomposition; radial basis function interpolation is then trained to map input parameters to the reduced coefficients, enabling rapid reconstruction of the full-field actuator response. The reconstructed responses are compared with FEM simulations for error analysis and validated against experiments on a custom-fabricated pneumatic network actuator. Results demonstrate that, within the sampled operating domain, the proposed method enables accurate, near real-time (calculation time < 1 s) predictions of bending deformations, spatial stress and displacement distributions, and tip contact forces, thereby realizing a digital twin of the actuator. Furthermore, a digital twin of a multi-actuator grasping system is demonstrated, highlighting the effectiveness of the method in creating efficient digital twins for soft robotic systems with strong potential for closed-loop control, performance monitoring, and decision-making.

1. Introduction

Digital twins are an emerging paradigm across engineering disciplines, aiming to construct high-fidelity virtual representations that mirror and continuously synchronize with physical systems (Tao and Qi, 2019; Tao et al., 2022). By integrating predictive models with physical-state and sensor data through continuous information exchange with the physical system, digital twins enable condition monitoring, performance prediction, fault diagnosis, decision support, and ultimately design and operation optimization of mechanical systems (Lai et al., 2023; He et al., 2025), making them increasingly important across industries such as aerospace, civil engineering, and smart manufacturing (Li et al., 2023; Liu et al., 2021). However, their application to soft robotics is still limited, mainly due to the challenge of developing models of soft actuators that are both accurate and computationally efficient for real-time use (Jin et al., 2020; Mengaldo et al., 2022).

Soft pneumatic actuators (SPAs) are fundamental components of soft robotics, valued for their intrinsic compliance, adaptability, and safety in unstructured environments. Typically fabricated by embedding fluidic channels within elastomeric matrices, SPAs are actuated by pressurizing internal pneumatic networks, enabling bending, twisting, and other complex deformations (Xavier et al., 2022). They have been widely deployed in soft grippers (Ilievski et al., 2011; Xie et al., 2020), crawling robots (Shepherd et al., 2011), and a range of other soft robotic systems (Gorissen et al., 2020; Pu et al., 2024). Despite their versatility, SPAs remain challenging to model and control due to their highly nonlinear, continuum-level deformation behavior, which arises from a complex interplay of actuator geometry, hyperelastic material properties, fluid–structure interactions, and environmental effects such as contact and friction (An et al., 2018). Analytical models, while computationally efficient, rely on simplifying assumptions that limit their predictive accuracy, particularly under large deformations or multi-point contact conditions (Wang et al., 2023; Gu et al., 2021; Zhong et al., 2021). Finite element modeling (FEM) offers a more

* Corresponding author at: Robotic Satellite Key Laboratory of Sichuan Province, Key Laboratory of Advanced Spatial Mechanism and Intelligent Spacecraft, Ministry of Education, School of Aeronautics and Astronautics, Sichuan University, Chengdu 610065, People's Republic of China.

E-mail address: anning@scu.edu.cn (N. An).

https://doi.org/10.1016/j.ijsolstr.2026.114190
Received 11 January 2026; Received in revised form 26 June 2026; Accepted 3 July 2026
Available online 9 July 2026

comprehensive and physically accurate approach, enabling detailed predictions of stress distributions, full-field deformations, and nonlinear material responses (Moseley et al., 2016; Xavier et al., 2021). This accuracy, however, comes at a high computational cost, making FEM impractical for time-sensitive tasks such as closed-loop control, rapid design iteration, or integration into digital twin frameworks.

Surrogate modeling offers a promising approach to accelerate simulations by learning data-driven mappings from simulation-based inputs to outputs. In this framework, high-fidelity FEM simulations are conducted to generate paired input–output datasets, which are then used to construct surrogate models, including artificial neural network (ANN) models, radial basis functions (RBFs), Kriging, Gaussian process regression, and Bayesian models. Once trained, these models can deliver near-instantaneous predictions of actuator performance, dramatically reducing FEM computation costs and enabling efficient design, optimization, and control. These approaches have been widely used in data-driven soft robot modeling (Chen et al., 2024) and inverse design problems (Chen et al., 2026). However, most surrogate models used in soft robotic design are formulated as mappings between a small number of input parameters and low-dimensional outputs. For instance, Liu et al. (2022) trained an ANN-based surrogate model using simulation data from the Simulation Open Framework Architecture (SOFA) to map two geometric design parameters of a soft pneumatic finger to center-of-gravity offset and bending reaction force. Wang et al. (2024) employed Gaussian process surrogate models within the Fin-Bayes framework to map eight geometric design variables of fin-ray fingers to two objectives, compliance and output force, for multi-objective Bayesian optimization. Xiao et al. (2025) developed RBF and Kriging surrogate models for a vacuum-powered soft bending actuator to relate actuating pressure and chamber-wall thickness parameters to bending curvature for programmable shape matching. Zhang et al. (2022) developed a neural network-based joint surrogate model that maps pressure, two force components, and torque to the coordinates of ten centerline anchor points, enabling fast prediction of pneumatic joint deformation, although prediction errors can accumulate when multiple joints are assembled into a gripper system. Collectively, these studies demonstrate the efficiency of surrogate modeling for rapid performance evaluation and design exploration, but they remain largely limited to low- or moderate-dimensional outputs. They are therefore not directly applicable to full-field prediction tasks involving thousands of nodal displacements, stresses, or strains. Fast and accurate prediction of full-field stress, strain, or deformation therefore requires an intermediate dimensionality-reduction strategy that retains the dominant mechanical information while avoiding direct mapping to thousands of nodal or elemental outputs.

Reduced-order modeling (ROM) provides such a strategy by extracting dominant deformation modes from high-dimensional simulation data and representing system behavior in a compact, lower-dimensional subspace. ROM techniques thereby reduce the dataset size required for surrogate modeling while retaining key physical characteristics. Proper orthogonal decomposition (POD), one of the most widely used ROM techniques, has demonstrated effectiveness in diverse fields. A classic example is eigenfaces in facial recognition, where principal component analysis (PCA) compresses high-dimensional image data into a small number of orthogonal basis vectors, enabling efficient representation and recognition of human faces (Muller et al., 2004). In engineering over the past years, POD has been successfully applied to problems such as fluid flow (Taira et al., 2020), heat transfer (Wang et al., 2012), solid structural dynamics (Ayoub et al., 2022), and fluid–structure interactions (Liberge and Hamdouni, 2010). Specifically, recent studies have begun exploring the integration of ROM and surrogate modeling to develop digital twins for various mechanical systems. Aversano et al. (2019) combined PCA with Kriging to develop a ROM-surrogate modeling framework for combustion systems. This approach constructs accurate and computationally efficient ROMs from a limited set of high-fidelity computational fluid dynamics simulations, enabling rapid parameter exploration and uncertainty quantification for digital twins. Lai et al. (2023) present a digital twin framework that combines load identification, multi-fidelity surrogate modeling, and online fatigue damage estimation, offering a promising approach for structural health monitoring, though its generalizability would benefit from validation across broader classes of structures. Yang et al. (2024) developed a digital twin for monitoring thermal stratification in pressurizer surge lines in nuclear engineering. By integrating POD with an artificial neural network, they mapped a set of design parameters to the full-field thermal and stress distributions of the surge lines, enabling real-time predictions of thermo-fluid–structure interaction under parametric variations. Collectively, these studies demonstrate the effectiveness of integrating ROM with surrogate models for achieving near real-time full-field state estimation of mechanical structures and systems.

Inspired by these advances, this work investigates a framework that combines POD-based ROM with surrogate modeling for SPAs, a field that has received relatively little attention. Goury and Duriez (2018), Goury et al. (2021) made the first attempt to integrate ROM with real-time FEM simulations using SOFA. While SOFA enables fast, interactive simulations (Schegg et al., 2023), its accuracy is inherently limited by the trade-off between real-time performance and physical fidelity (Ferrentino et al., 2022; Liu et al., 2022). High-speed, interactive simulations may sacrifice detail in material behavior, mesh resolution, contact handling, and actuation physics, making them less accurate than high-fidelity FEM tools like Abaqus. In contrast, Abaqus is an industry-grade, general-purpose FEM solver known for its robustness and extensive material library, enabling high-fidelity modeling of nonlinear deformations, hyperelasticity, and complex contact conditions (Polygerinos et al., 2015; Wang et al., 2016). To the best of our knowledge, this is the first work to integrate ROM and surrogate modeling with high-fidelity Abaqus simulations for SPAs, combining engineering-grade accuracy with real-time predictive capability. By deriving reduced-order and surrogate models directly from Abaqus simulations, our approach preserves engineering-grade accuracy while achieving real-time capability, bridging the gap between interactive control frameworks and industrially validated predictive models. The proposed method delivers computationally efficient, high-fidelity models for real-time full-field deformation prediction, thereby supporting predictive digital twin capabilities for soft robotic systems. Because the surrogate is trained from a finite set of FEM simulations, this predictive capability should be interpreted within the sampled training domain rather than as unrestricted extrapolation to arbitrary unseen conditions. Nevertheless, by enabling real-time full-field reconstruction from high-fidelity FEM data, the framework can serve as a basis for soft-robot digital twins that could be extended beyond the training domain in the future. Using a classical pneumatic networks (PneuNets) actuator and gripper as examples, this paper details the development of a digital twin by integrating ROM and surrogate models, with experimental validation showing good agreement between predictions and measured performance.

Fig. 1 illustrates the soft robotic digital twin concept. Physical sensors measure the actuation pressure and the distance from the actuator to the ground, and these parameters are fed into the digital twin to compute real-time deformation and contact behavior. A visualization system reconstructs stress, strain, and displacement at each node and element in real time, yielding a FEM-like representation of the physical system with real-time performance. The method can be summarized in four steps: (i) develop a high-fidelity FEM model of the actuator; (ii) perform extensive parametric studies to collect deformation data under varying pressures and distances; (iii) apply POD to extract principal components, reducing the high-dimensional FEM data (coordinates, displacements, stress, strains, contact forces, etc.) into a small set of POD parameters and corresponding eigenmodes that capture full-field deformation; and (iv) construct a surrogate model mapping physical inputs, such as pressure and distance, to the POD parameters, which

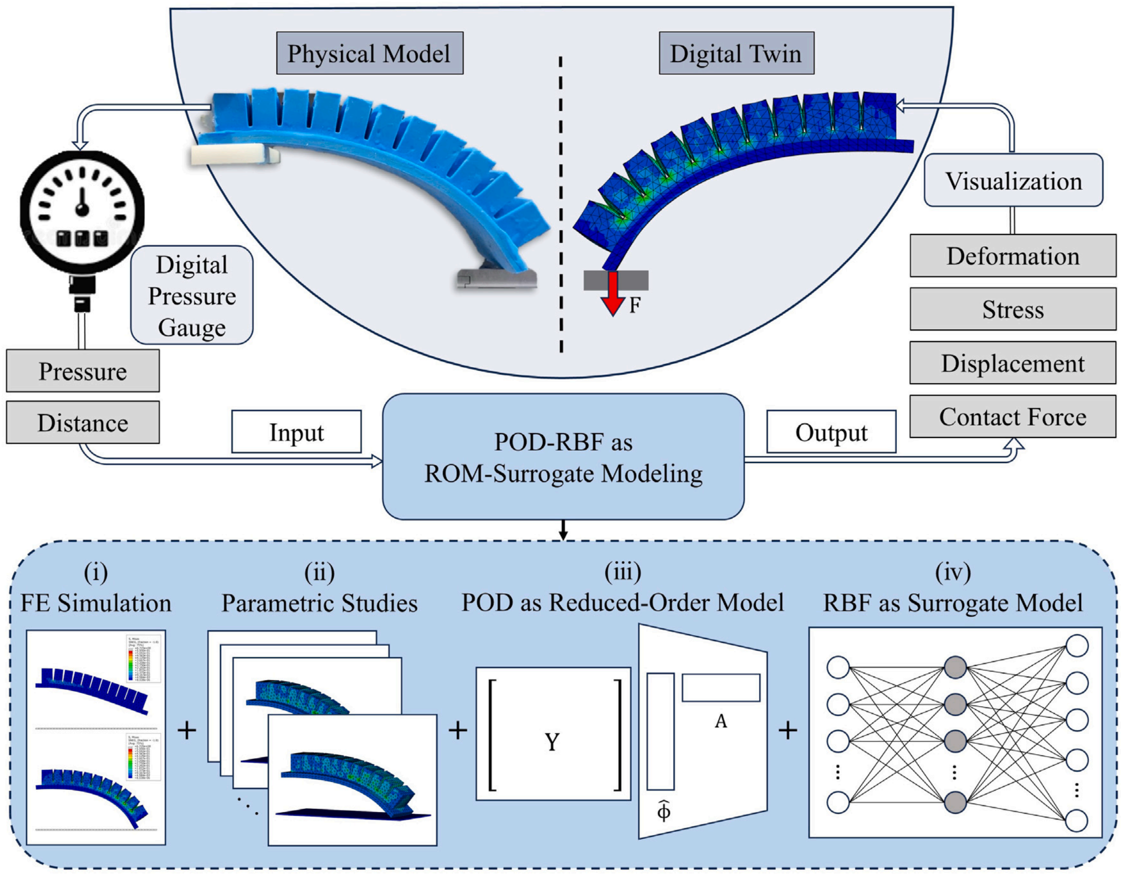

Fig. 1. Flowchart of the proposed ROM-surrogate modeling framework for developing a digital twin of SPAs. Actuation pressure measured by a sensor is fed into the digital twin to predict real-time bending and contact deformations. The full-field response is reconstructed and visualized in a FEM-like representation. The framework comprises four steps: (i) FEM simulation, (ii) parametric studies, (iii) POD-based reduced-order modeling, and (iv) RBF-based surrogate modeling.

can then be used to reconstruct the full-field deformation for real-time prediction and visualization.

The paper is organized as follows. Section 2 details the geometry and fabrication of SPAs, along with the FEM techniques and experimental methods used to characterize their bending deformations and contact forces. Section 3 introduces the theory of POD, RBFs, and the POD–RBF hybrid modeling strategy. Section 4 presents the error analysis and several validation examples to demonstrate the accuracy and efficiency of the proposed method as a digital twin for SPAs, followed by a multi-actuator grasping case as a demonstration. Finally, Section 5 summarizes the key findings and outlines directions for future work.

2. Soft pneumatic actuators

This section introduces the SPA and presents the development and validation of a FEM model that captures its deformation and contact behavior under internal pressure. This validated high-fidelity model provides the foundation for the subsequent reduced-order and surrogate modeling.

2.1. Design

The SPA considered in this work follows the classical PneuNets design of Mosadegh et al. (2014), which has been extensively studied since. It is used here as a representative example to demonstrate the development of a digital twin for soft actuators using reduced-order and surrogate modeling approaches. Fig. 2 illustrates the design, fabrication, and deformation behavior of the PneuNets actuator. Fig. 2(A) shows two actuators grasping an object. Each actuator consists of a soft elastomeric body with embedded pneumatic channels and an inextensible, strain-limiting layer formed by embedding a sheet of paper within the elastomer, as shown in Fig. 2(B). Upon pressurization by pumping fluid into the internal channels, the chambers expand, and adjacent channel walls come into contact, causing the actuator to bend, as depicted in Fig. 2(C). The grasping performance of the gripper depends on the contact interaction between each actuator and the object, including the normal contact interaction and frictional resistance at the contact interface. Therefore, the design of a PneuNets actuator must account for both its bending behavior and its contact interaction with the target object, the latter being strongly influenced by the initial distance between the actuator and the object (Zou et al., 2024), as shown in Fig. 2(D).

2.2. Experiment

The actuator considered in this study was fabricated using an injection molding process. The body was cast from silicone elastomer (Ecoflex Sil-950 A and B, Smooth-On, USA). Molds for both the main body and bottom layer were produced using 3D-printed resin (8200Pro, Wenext Technology, China). Ecoflex Sil-950 A and B were measured and mixed at a 1 : 10 ratio in a clean container. To fabricate the main body, the mixture was poured into the mold and cured in a vacuum oven. For the bottom layer, the mold was half-filled with the mixture and partially cured to form a half-thickness layer. A sheet of standard printing paper, cut to size, was then placed on top of this partially cured layer as a strain-limiting element. The remaining mixture was poured to complete the layer, and the cured main body was positioned on top. The components were then cured and bonded to form the complete SPA. Uniaxial tensile tests were performed to characterize the hyperelastic

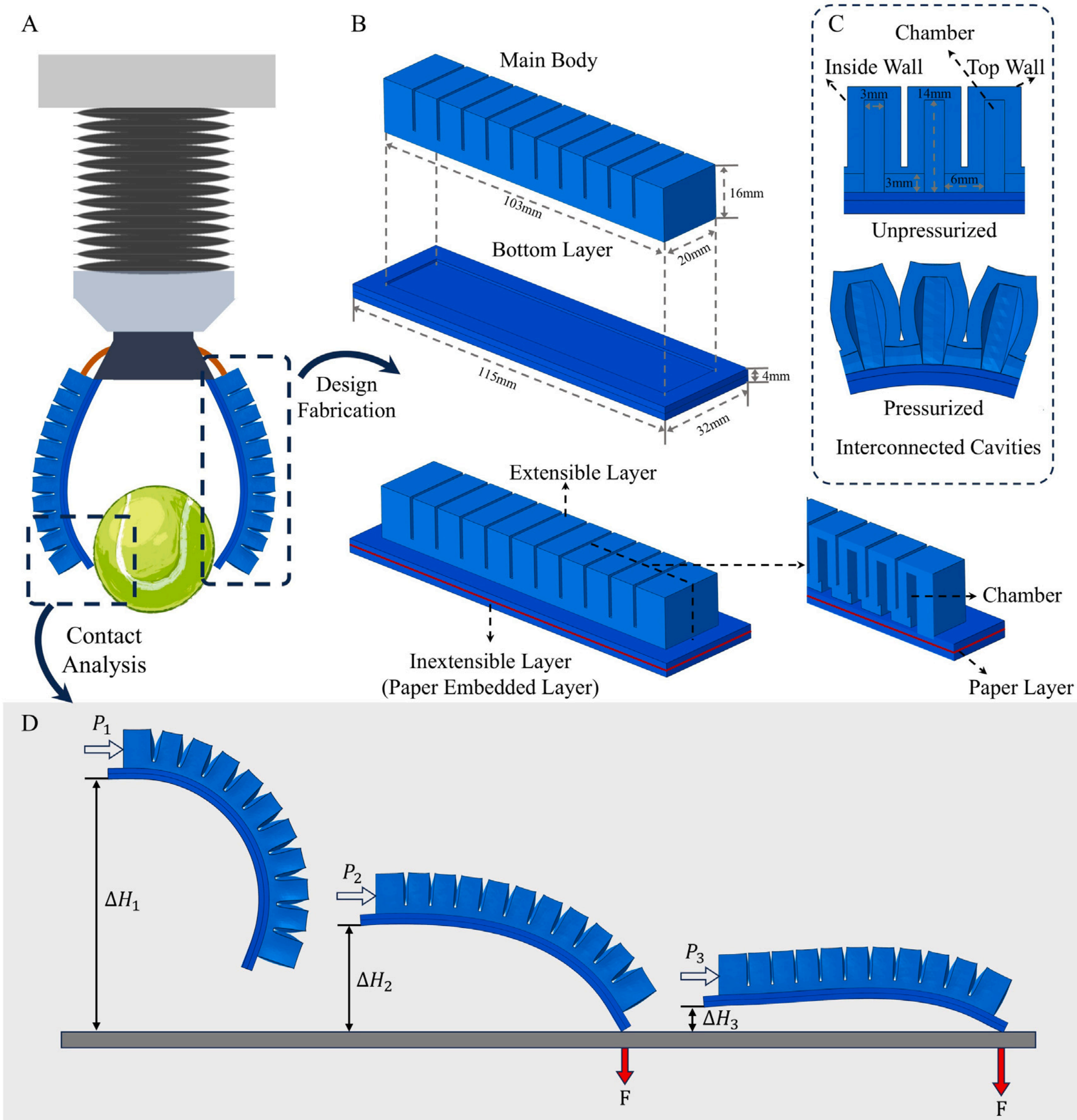

Fig. 2. Design, fabrication, and actuation of SPAs. (A) Two SPAs functioning as a soft gripper for grasping. (B) Geometric design of the pneumatic network with dimensions. The actuator consists of a soft elastomeric body with embedded pneumatic channels and an inextensible, strain-limiting layer formed by embedding paper within the elastomer. (C) Pressurization of the pneumatic channels with air or fluid causes the chambers to expand, resulting in actuator bending. (D) Schematic illustration of the actuator's bending and contact behavior under pressurization.

behavior of the elastomer. Details of the actuator fabrication process and material characterization are provided in an earlier study by the authors (Lu et al., 2026); these details are omitted here for brevity.

To experimentally characterize the response of the pneumatic actuator, a test setup was developed to measure both its bending and contact behavior under pressurization. As shown in Fig. 3(A), a syringe pump (LSP01-3A, LongerPump, UK) was used to deliver fluid into the actuator at a controlled rate of 125 mL/min. The internal pressure was monitored using a digital pressure gauge (YK-120B, Shelok, China) connected to a computer for data acquisition. A digital camera (SONY α6000) was positioned in front of the actuator to capture its deformation during inflation. Bending behavior was measured in a water tank to eliminate gravitational effects, with water used as the working fluid. In contrast, contact force measurements were conducted in air, where the actuator was inflated pneumatically. A load cell (ZNZV6-T1-485, CHINOSENSOR, China) was placed parallel to the actuator at a fixed distance H, enabling continuous monitoring of the reaction force exerted by the air-pressurized actuator under combined gravitational and pneumatic loading conditions. We note that this experimental setup has also been used in a previous study (Lu et al., 2026) to investigate the effect of elastomer viscosity on the bending behavior of the actuator. In the present work, the same setup is used to characterize the actuator response while focusing on its hyperelastic behavior.

2.3. FEM model

To compute the bending and contact mechanics of SPAs, high-fidelity 3D FEM models were developed using Abaqus 2020. Fig. 3(B) shows the FEM model with its mesh representation and boundary conditions. The actuator body was discretized using 10-node quadratic tetrahedral hybrid elements (`C3D10H`), while the embedded paper layer was modeled with 3-node quadratic triangular shell elements (`STRI65`). To capture the actuator-plate contact behavior and facilitate extraction of reaction forces on the load cell, a rigid plate was positioned parallel to the actuator with an initial gap ΔH. The plate

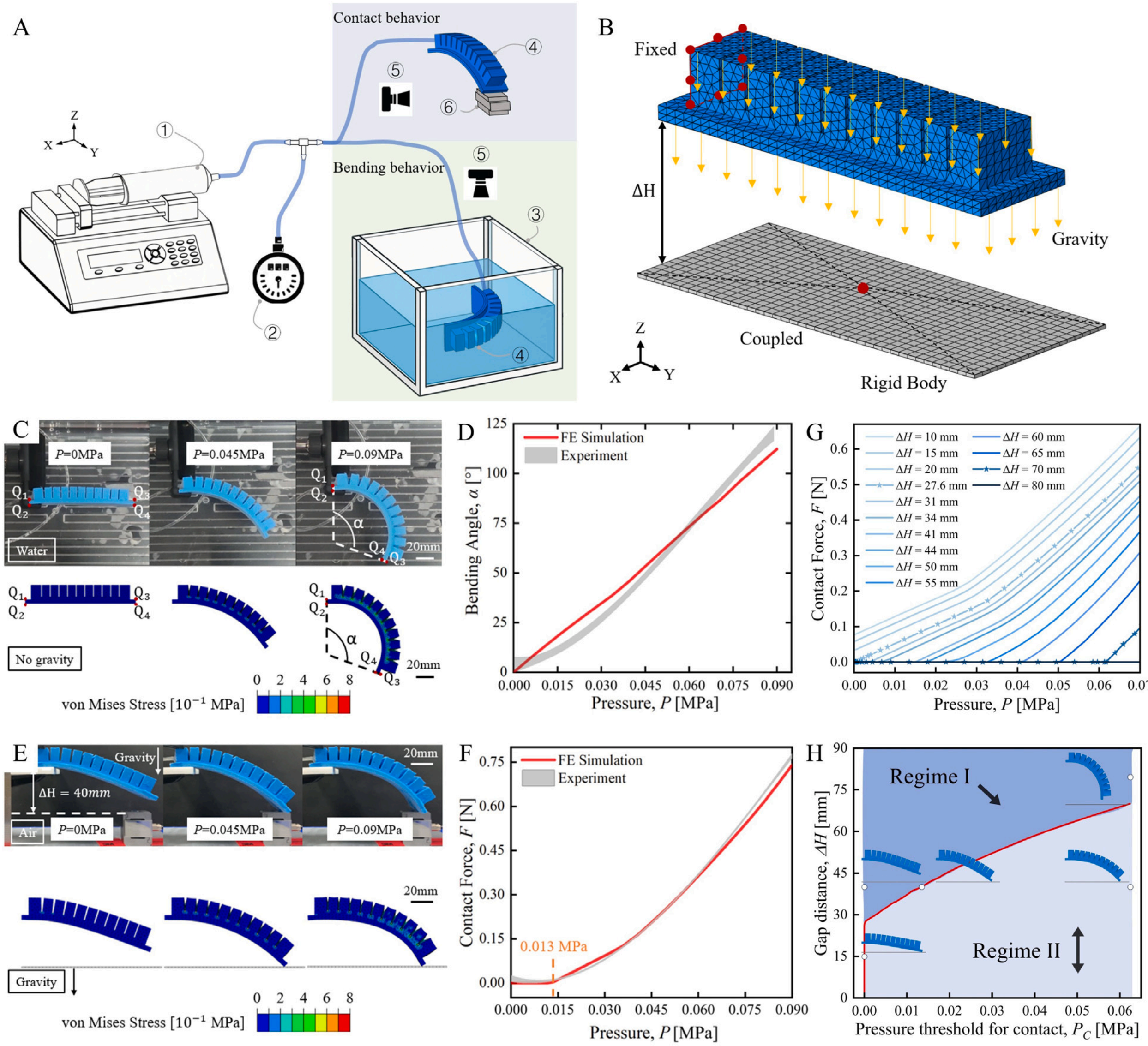

Fig. 3. Experimental setup, FEM model, and validation of the SPA. (A) Experimental setup for inflation tests, showing components used to measure bending angle and contact force versus internal pressure: (1) syringe pump; (2) digital pressure gauge; (3) water tank; (4) soft actuator; (5) digital camera; (6) load cell. Bending was measured in water to remove gravity; contact behavior was measured in air. (B) FEM mesh in the uninflated state; a rigid plate beneath measures contact forces. (C) Bending snapshots in water (gravity neglected). (D) Bending angle versus inflation pressure (0–0.09 MPa). (E) Bending and contact snapshots in air (gravity included). (F) Contact force versus pressure (0–0.09 MPa); contact begins above 0.013 MPa. (G) Parametric study of the effect of ΔH on the contact force versus inflation pressure response, obtained from FEM simulations. (H) Due to initial bending under gravity, each ΔH corresponds a particular pressure threshold P_c for the onset of contact. The system behavior is then divided into two regimes: regime I (no contact) and regime II (contact).

was meshed using reduced-integration 20-node hexahedral elements (C3D20R) and defined as a rigid body using the Abaqus Interaction module. A mesh-convergence study showed that key outputs – deformation, stress distribution, and reaction forces – were insensitive to further mesh refinement, resulting in a discretization with a total of 15 744 elements and 25 022 nodes for the actuator model. The left side of the actuator body was fully constrained, and the rigid plate was kinematically coupled to a fully fixed reference point, enabling the extraction of reaction forces at the reference point. Contact was modeled as self-contact on cavity walls and surface-to-surface interaction between the actuator and plate, with hard contact in the normal direction and frictionless tangential behavior.

The elastomer was modeled using the incompressible Gent hyperelastic material model (Gent, 1996), with the following strain–energy density function:

$$W = -\frac{\mu J_m}{2} \ln\left(1 - \frac{I_1 - 3}{J_m}\right), \tag{1}$$

where μ is the small-strain shear modulus, J_m is a material parameter associated with limiting stretch, and $I_1 = \mathrm{tr}(\mathbf{F}^T\mathbf{F})$, with $\mathbf{F}$ denoting the deformation gradient. The uniaxial tensile response of Ecoflex Sil-950 was experimentally characterized and fitted to this model, yielding parameters $(\mu, J_m) = (0.8\ \mathrm{MPa}, 6.0)$. The embedded paper layer was represented as a linear elastic material with density $\rho = 750\ \mathrm{kg/m^3}$, Young's modulus $E = 6.5$ GPa, and Poisson's ratio $\nu = 0.2$. The plate was treated as a rigid body to represent structural steel, whose stiffness exceeds that of the soft actuator by several orders of magnitude. Gravity was applied in the negative z-direction with $g = 9.81\ \mathrm{m/s^2}$; simulations performed in a water tank omitted gravitational loading. The internal pneumatic cavity was modeled as a fluid-filled chamber (the Fluid Cavity option in Abaqus) containing either air ($\rho_{\mathrm{air}} = 1.225\ \mathrm{kg/m^3}$) or water ($\rho_{\mathrm{water}} = 1000\ \mathrm{kg/m^3}$). Actuation was simulated by applying a prescribed cavity pressure P to drive inflation. All simulations were performed using the *Static General procedure in Abaqus, with geometric nonlinearity enabled. A custom Python script was developed to extract nodal coordinates (X, Y, Z), von Mises stress S, displacement magnitude U, and contact force F at each pressure increment. The extracted data were systematically stored to facilitate the development of the digital twin of the actuator.

2.4. Validation

Before constructing the digital twin, the FEM model was validated against experimental measurements of both bending and contact behavior. Fig. 3(C) shows bending snapshots of the actuator from experiments and FEM simulations. In the water tank, buoyancy compensates for gravity, allowing the actuator's weight to be neglected. Fig. 3(D) compares the bending angle as a function of inflation pressure, showing good overall agreement and supporting the accuracy of the FEM model in predicting the actuator's bending deformation over the main deformation range. The initial flat region in the experimental bending-angle curve at very low pressure is not fully reproduced by the FEM model. This discrepancy is mainly attributed to experimental pressure-transmission and measurement effects during the early inflation stage, including tubing compliance, local chamber filling, small trapped bubbles, and pressure-gauge resolution. In contrast, the FEM model applies an idealized uniform cavity pressure directly to the internal chamber surfaces, so the simulated actuator responds immediately to the prescribed pressure. This discrepancy is therefore mainly associated with the experimental pressure-delivery process at early inflation and does not affect the model's ability to capture the dominant bending and contact response at moderate and high pressures. Fig. 3(E) presents bending and contact snapshots of the actuator at various inflation pressures in air, where gravity is considered. At zero inflation, the actuator exhibits a slight initial bend. As air is pumped into the channels, the actuator bends further until its tip contacts the load cell, which then measures the contact force. Fig. 3(F) compares the contact force as a function of inflation pressure. Contact occurs at an inflation pressure of approximately 0.013 MPa, and both experimental measurements and FEM predictions show excellent agreement.

It should be noted that for a given actuator design, the contact force depends not only on the inflation pressure but also on the initial gap distance between the actuator and the plate, ΔH. FEM simulations were performed to investigate the effect of ΔH on the contact force versus inflation pressure response, as summarized in Fig. 3(G). The results indicate that, due to the actuator's bending under gravity, the initial sag of the actuator tip is approximately 27.6 mm. For $\Delta H < 27.6$ mm, the actuator contacts the plate even before inflation. For 27.6 mm $<$ $\Delta H < 70$ mm, contact occurs only after the inflation pressure reaches a threshold pressure P_c. For $\Delta H > 70$ mm, no contact occurs even at maximum bending, as the plate is positioned too far from the actuator tip. In the contact cases, the contact force increases rapidly once contact occurs and pressure continues to rise. This behavior can be divided into two regimes, denoted as Regime I and Regime II in Fig. 3(H). For a given ΔH, Regime I corresponds to pressures below P_c, where no contact takes place, whereas Regime II corresponds to pressures above P_c, where contact is established. These regimes should be treated separately when constructing the actuator digital twin, as contact introduces highly nonlinear behavior that significantly influences the system's response.

3. POD–RBF hybrid strategy

Having validated the accuracy of the FEM model, we next develop the POD–RBF framework used to construct the actuator digital twin. The water-tank bending tests were used to validate the gravity-free bending response of the FEM model, whereas the subsequent POD–RBF digital-twin construction is based on the air-contact configuration, because this setting captures both gravity-induced deformation and actuator–object contact forces. This section describes how high-dimensional FEM outputs are reduced into compact POD coefficients and how an RBF surrogate model is trained to map physical input parameters to these coefficients. The resulting POD–RBF model enables rapid reconstruction of full-field displacement, stress, strain, and contact responses for new operating conditions.

3.1. POD

The initial stage of the POD procedure involves constructing a snapshot matrix from simulation data generated through parametric FEM analyses. As discussed in Fig. 3(H), in *Regime I*, where no contact occurs, the inflation pressure P serves as the sole input parameter. In *Regime II*, where contact with the plate is present and influenced by both the inflation pressure and the initial gap distance ΔH, the parameter pair $(P, \Delta H)$ constitutes a two-dimensional input vector. For each sampled input, the FEM model computes full-field nodal responses across the discretized actuator domain. The recorded variables include five quantities at each node: nodal coordinates (X, Y, Z), von Mises stress S, and displacement magnitude U. Since the FEM model contains 25,022 nodes, each input parameter set corresponds to a snapshot vector with 125,110 entries. Therefore, the surrogate problem is not a trivial interpolation of scalar outputs; it requires mapping low-dimensional physical inputs to a high-dimensional full-field mechanical response. POD is introduced to reduce the order of the snapshot matrix before surrogate modeling, so that the RBF network predicts a compact set of modal coefficients rather than the original high-dimensional response vector. These snapshot vectors are assembled into the matrix $\mathbf{Y}_{\text{snap}}$, which serves as the foundation for POD-based model reduction:

$$\mathbf{Y}_{\text{snap}} = \left[\, \mathbf{Y}(\mathbf{x}_1)\ \mathbf{Y}(\mathbf{x}_2)\ \cdots\ \mathbf{Y}(\mathbf{x}_m) \,\right] \in \mathbb{R}^{n\times m}, \tag{2}$$

where $\mathbf{Y}_{\text{snap}}$ is the snapshot matrix, $n = 125,110$ is the length of each snapshot vector based on the extracted nodal quantities, and m is the total number of simulation cases.

To reduce the dimensionality of the output data, we apply singular value decomposition (SVD) to the snapshot matrix:

$$\mathbf{Y}_{\text{snap}} \;=\; \mathbf{\Phi}\,\mathbf{\Sigma}\,\mathbf{V}^{\mathrm{T}}, \tag{3}$$

where the terms are defined as follows:

- $\mathbf{\Phi} \in \mathbb{R}^{n\times n}$ contains the left singular vectors (POD modes),
- $\mathbf{\Sigma} = \operatorname{diag}(\sigma_1, \ldots, \sigma_q) \in \mathbb{R}^{q\times q}$ is the diagonal matrix of singular values, with $q = \min(n, m)$,
- $\mathbf{V} \in \mathbb{R}^{m\times m}$ contains the right singular vectors.

A truncated POD basis $\hat{\mathbf{\Phi}} \in \mathbb{R}^{n\times \ell}$ is formed by retaining only the first ℓ modes, which can be selected according to a relative truncation error criterion:

$$\varepsilon(\ell) \;=\; 1 - \frac{\sum_{j=1}^{\ell} \sigma_j^2}{\sum_{j=1}^{q} \sigma_j^2}, \tag{4}$$

where σ_j is the jth singular value. The minimum ℓ is chosen such that $\varepsilon(\ell) \le 0.01$, ensuring that the reduced-order representation captures at least 99% of the original data's variance.

Using the truncated POD basis $\hat{\mathbf{\Phi}}$, each high-dimensional FEM snapshot $\mathbf{Y}(\mathbf{x}_i) \in \mathbb{R}^{n\times 1}$ is projected onto a reduced-order subspace, yielding a low-dimensional representation of size ℓ:

$$\mathbf{A}(\mathbf{x}_i) = \hat{\mathbf{\Phi}}^{\mathrm{T}}\mathbf{Y}(\mathbf{x}_i) \in \mathbb{R}^{\ell\times 1}, \tag{5}$$

The reduced-order dataset is assembled as

$$\mathbf{A} = \left[\mathbf{A}(\mathbf{x}_1)\ \mathbf{A}(\mathbf{x}_2)\ \cdots\ \mathbf{A}(\mathbf{x}_m)\right] \in \mathbb{R}^{\ell\times m}. \tag{6}$$

This projection reduces the dimensionality of each output snapshot from n to ℓ, while preserving most of the system's essential features. The reduced coefficients in $\mathbf{A}$ are the POD coordinates (modal amplitudes) that encode the dominant deformation, stress, and displacement characteristics of the system. The RBF surrogate model can then be trained to map the parameter space $\mathbf{x} \mapsto \mathbf{A}(\mathbf{x})$. Once trained, this surrogate predicts the reduced coefficients $\mathbf{A}^*$ for any new input parameter set $\mathbf{x}^*$. The full-field solution is subsequently reconstructed in the original high-dimensional space using the truncated POD basis:

$$\mathbf{Y}^* = \hat{\boldsymbol{\Phi}}\,\mathbf{A}^*. \tag{7}$$

The reconstructed full-field response is then visualized using the post-processing software Tecplot. This workflow achieves significant computational efficiency by performing learning and prediction in a low-dimensional latent space while retaining the accuracy necessary for high-fidelity reconstruction.

3.2. RBF neural networks

The RBF neural network is employed to establish a mapping between the input parameter vector $\mathbf{x}_i$ and the corresponding POD coefficient vector $\mathbf{A}(\mathbf{x}_i)$ using a set of radial basis functions:

$$\mathbf{A}(\mathbf{x}_i) \approx \sum_{k=1}^{m} \alpha_k\, g_k(\mathbf{x}_i), \tag{8}$$

where α_k are weighting coefficients and $g_k(\mathbf{x}_i)$ are the selected basis functions.

Using the linear spline RBF $g_k(\mathbf{x}_i) = \|\mathbf{x}_k - \mathbf{x}_i\|$, we define the hidden-layer column vector

$$\mathbf{G}_i = \left[g_1(\mathbf{x}_i), g_2(\mathbf{x}_i), \dots, g_m(\mathbf{x}_i)\right]^{\mathrm{T}} \in \mathbb{R}^{m\times 1}. \tag{9}$$

Stacking these for all training samples yields the square interpolation matrix

$$\mathbf{G} = \left[\mathbf{G}_1, \mathbf{G}_2, \dots, \mathbf{G}_m\right] \in \mathbb{R}^{m\times m}. \tag{10}$$

The mapping can be expressed in matrix form as

$$\mathbf{A}(\mathbf{x}_i) \approx \mathbf{B}\mathbf{G}_i, \tag{11}$$

where $\mathbf{B} \in \mathbb{R}^{\ell\times m}$ contains the coefficients of the linear combinations. Since the POD coefficients $\mathbf{A}(\mathbf{x}_i)$ are obtained from high-fidelity simulations, $\mathbf{B}$ is determined as

$$\mathbf{B} = \mathbf{A}\mathbf{G}^{-1}. \tag{12}$$

For a new parameter input $\mathbf{x}^*$, we first construct

$$\mathbf{G}^* = \left[g_1(\mathbf{x}^*), g_2(\mathbf{x}^*), \dots, g_m(\mathbf{x}^*)\right]^{\mathrm{T}}, \tag{13}$$

and then compute the predicted POD coefficient vector as

$$\mathbf{A}^* = \mathbf{B}\mathbf{G}^*. \tag{14}$$

This framework provides an efficient mapping $\mathbf{x}_i \mapsto \mathbf{A}(\mathbf{x}_i)$, enabling rapid prediction of low-dimensional POD representations from input parameters.

3.3. Training and prediction workflow

The POD–RBF training and prediction workflow for the SPA, as illustrated in Fig. 4, is summarized as follows:

(i) Sample the parameter space using Latin hypercube sampling to provide a space-filling distribution of input parameters $\mathbf{x}$. Recall that there are two regimes depending on whether contact occurs. In Regime I, only one parameter, P, is varied from 0 to 0.09 MPa, generating a total of 19 samples, with 17 used for training and 2 for testing. In Regime II, two parameters are considered: P varies from 0 to 0.09 MPa, and ΔH varies from 10 to 50 mm, generating 87 samples, with 85 used for training and 2 for testing. The sufficiency of these training datasets is evaluated in Section 4.1 by reducing the number of training samples and examining the resulting prediction error.

(ii) For each sampled parameter set, perform high-fidelity FEM simulations. Extract the field variables at each node and assemble the full-order snapshot matrix $\mathbf{Y}_{\text{snap}}$ for training and the test snapshot matrix $\hat{\mathbf{Y}}$ for testing, respectively, as described in Eq. (2).

(iii) Perform SVD on the full-order training snapshot matrix $\mathbf{Y}_{\text{snap}}$, extract the truncated POD basis $\hat{\boldsymbol{\Phi}}$, and compute the reduced-order POD coordinates matrix $\mathbf{A}$ using Eqs. (3)–(5).

(iv) Construct the RBF surrogate model by forming the interpolation matrix $\mathbf{G}$ from the training inputs $\mathbf{x}$ and solving for the coefficient matrix $\mathbf{B}$ using Eq. (12).

(v) For validation, the testing inputs $\hat{\mathbf{x}}$ are used to calculate the POD coordinates $\hat{\mathbf{A}}^*$ via Eq. (14), and the predicted full-order response $\hat{\mathbf{Y}}^*$ is subsequently reconstructed using Eq. (7). The predicted $\hat{\mathbf{Y}}^*$ is then compared with the FEM-calculated results $\hat{\mathbf{Y}}$ to assess the accuracy of the proposed method. Additionally, the mean-squared error (MSE) on the test set is employed to validate the truncation order ℓ: although the POD relative truncation error $\varepsilon(\ell) < 0.01$ provides an initial guideline, the final choice of ℓ is made to minimize the test-set MSE.

(vi) Upon receiving a new input $\mathbf{x}^*$, the reduced-order POD coefficients $\mathbf{A}^*$ are predicted using the RBF-based surrogate model via Eq. (14). The truncated POD basis $\hat{\boldsymbol{\Phi}}$ is then used to reconstruct the full-order data matrix $\mathbf{Y}^*$ via Eq. (7), which is subsequently visualized using the post-processing software Tecplot.

This POD–RBF hybrid framework produces a compact surrogate that (i) substantially reduces the dimensionality of the FEM outputs, (ii) provides an inexpensive, continuous mapping from input parameters to reduced states, and (iii) enables accurate reconstruction and visualization of full-field quantities for digital twin applications.

4. Results and discussion

4.1. Error analysis

We begin by analyzing the prediction error between the POD–RBF surrogate and the FEM-calculated results. These errors arise from two primary sources: the truncation error introduced during the POD process and the prediction error of the RBF surrogate model. As discussed in Eq. (4), the POD truncation error $\varepsilon(\ell)$ can be controlled to remain below 0.01 by selecting a sufficiently large number of POD modes ℓ for representing the high-dimensional snapshot matrix. However, once combined with the RBF surrogate, additional errors are introduced, necessitating a direct comparison between the POD–RBF-reconstructed high-dimensional snapshot matrix $\mathbf{Y}^*$ and the FEM-calculated matrix $\mathbf{Y}$ to assess the overall accuracy of the hybrid method.

To this end, an MSE metric is defined to quantify the discrepancy between the FEM-calculated test snapshot matrix $\hat{\mathbf{Y}}$ and the POD–RBF-reconstructed test snapshot matrix $\hat{\mathbf{Y}}^*$ over all test cases:

$$\text{MSE} = \frac{1}{n_{\text{test}}} \sum_{k=1}^{n_{\text{test}}} \frac{1}{n} \sum_{j=1}^{n} \left\| \hat{\mathbf{Y}}^*_{j,k} - \hat{\mathbf{Y}}_{j,k} \right\|^2, \tag{15}$$

where n_{test} is the number of test cases, n is the dimension of each snapshot vector, $\hat{\mathbf{Y}}_{j,k}$ denotes the FEM-calculated value of the jth quantity in the kth test case, and $\hat{\mathbf{Y}}^*_{j,k}$ is the corresponding POD–RBF prediction. This formulation provides a global error metric for evaluating the overall accuracy of the POD–RBF hybrid method.

Fig. 5 shows that as the number of POD modes used for dimensionality reduction increases, both the POD truncation error and the POD–RBF MSE decrease. For Regime I (non-contact cases), the number of POD modes is selected as $\ell = 4$ based on the combined trends in POD truncation error and test-set MSE, with the POD relative error approximately 1.0×10^{-12} and the POD–RBF MSE around 3.56×10^{-4}. For Regime II (contact cases), where the nonlinearity is more significant due to contact interactions, $\ell = 6$ is selected, yielding a POD relative

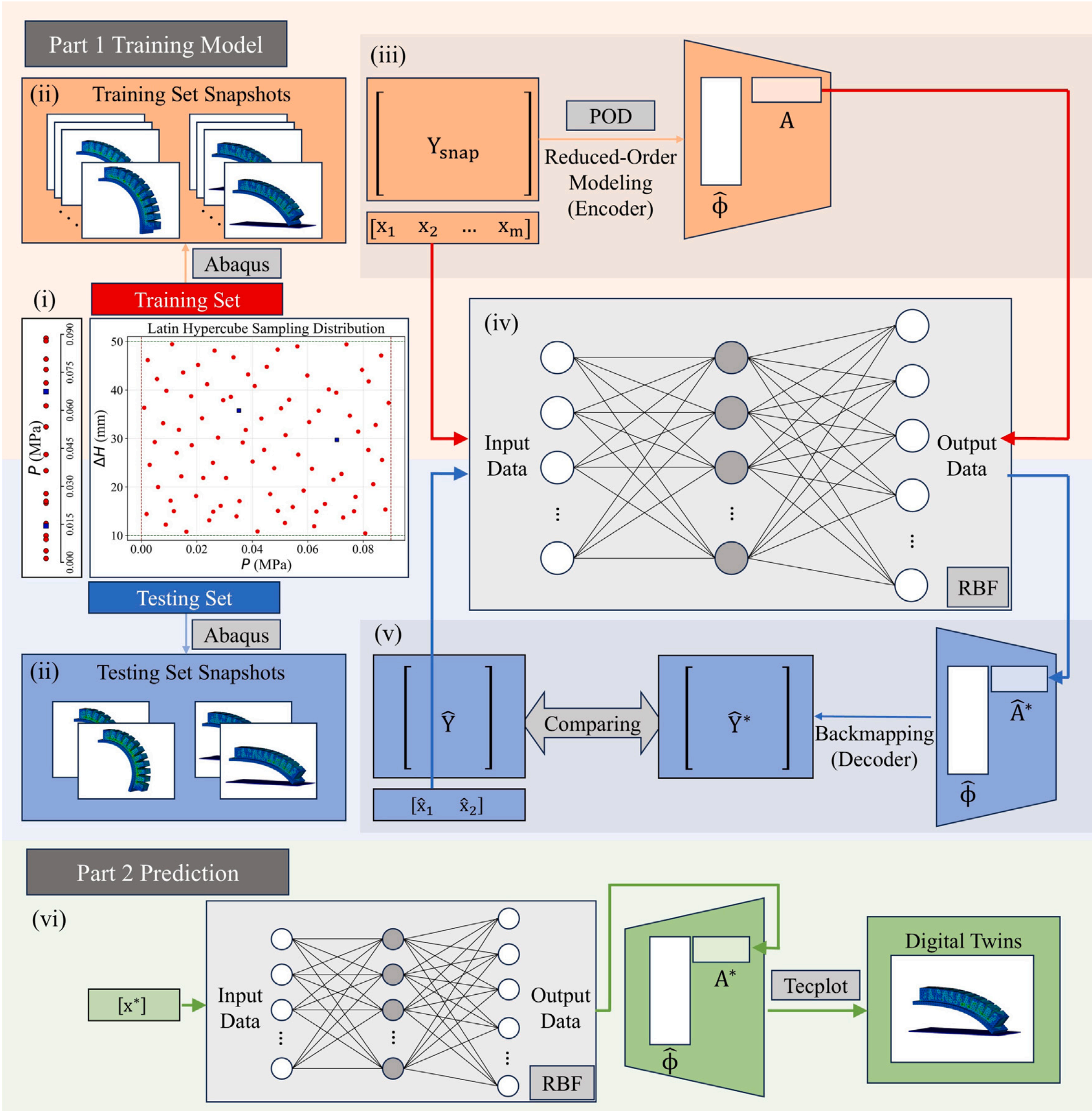

Fig. 4. Schematic illustration of the POD–RBF hybrid modeling framework used to develop a digital twin for the soft actuator.

error of 1.0×10^{-6} and a POD–RBF MSE of approximately 4.18×10^{-3}. In addition, Fig. 5(C,F) evaluates the influence of the number of training samples on the prediction accuracy of the POD–RBF surrogate. For Regime I, the MSE generally decreases as the number of training samples increases from 3 to 17, with a pronounced reduction when the training size increases from 6 to 9. This sharp decrease occurs because one of the additional training samples is located close to a testing point, indicating that the MSE can be sensitive to the spatial distribution of the training samples when the test set is limited. For Regime II, increasing the number of training samples from 20 to 85 leads to a monotonic reduction in the MSE, confirming that broader coverage of the two-dimensional $(P, \Delta H)$ parameter space improves the overall prediction accuracy. These results show that both the number and the distribution of training samples are important for constructing an accurate reduced-order surrogate model.

The retained POD modes were visualized using the Tecplot post-processing code. Physically, each high-dimensional deformation snapshot can be represented as a linear combination of the POD modes, meaning that the full-field deformation at all nodes is effectively reduced to a small set of POD coordinates. In Fig. 6, the four leading POD modes for Regime I (non-contact cases) and the six leading POD modes for Regime II (contact cases) are shown; these modes are subsequently used to reconstruct the full-field deformation snapshots of the actuator.

4.2. Verification and validation

As described in Section 3.1, the POD–RBF surrogate maps low-dimensional physical inputs to high-dimensional full-field mechanical responses. This section verifies the reconstructed fields against independent FEM testing samples in both Regime I and Regime II, while additional checks on extrapolation behavior and nearest-sample substitution are provided in the appendices.

Fig. 7 presents a comparison between the FEM results and POD–RBF predictions for two testing samples from Regime I, where no contact occurs. Fig. 7(A) shows the FEM results and POD–RBF predicted stress and displacement fields for test Case A ($P = 1.44 \times 10^{-2}$ MPa), along with the spatial distribution of the relative error in the deformed configuration. The relative error between the FEM results and the POD–RBF predictions is used to quantify the accuracy of the POD–RBF

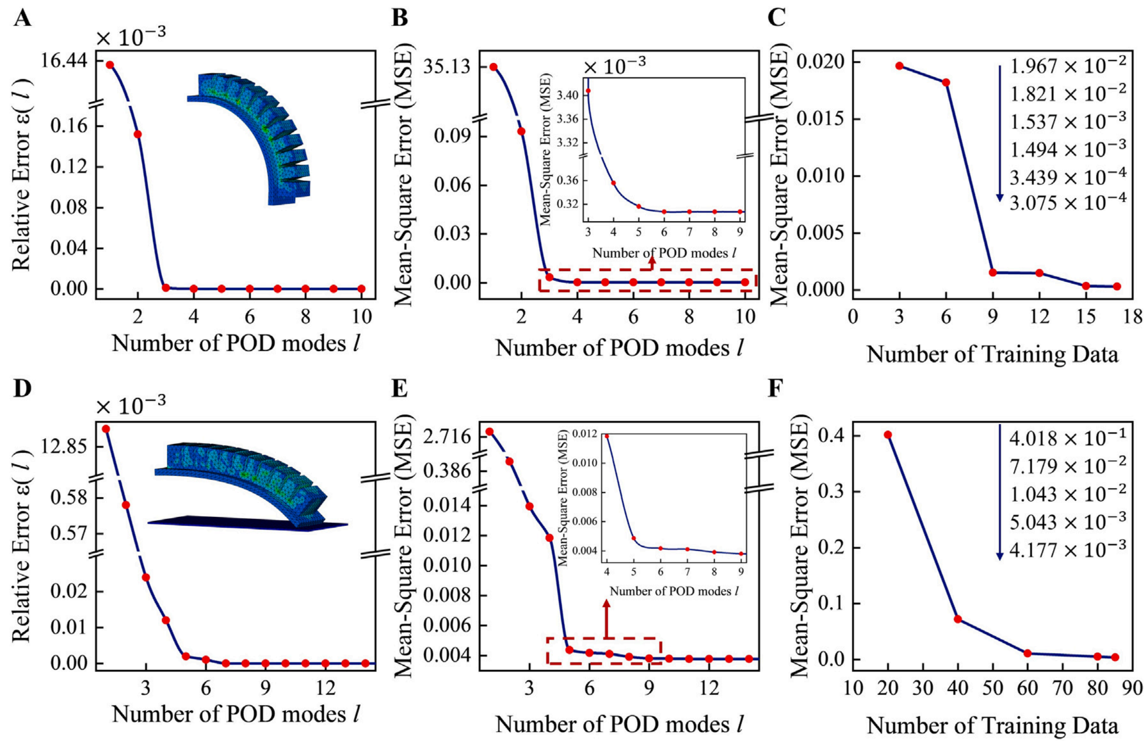

Fig. 5. Error analysis of the POD–RBF hybrid strategy. Evolution of the (A) POD truncation error and (B) POD–RBF MSE as a function of the number of truncated POD modes for Regime I (non-contact cases). (C) POD–RBF MSE as a function of the number of training samples for Regime I. Evolution of the (D) POD truncation error and (E) POD–RBF MSE as a function of the number of truncated POD modes for Regime II (contact cases). (F) POD–RBF MSE as a function of the number of training samples for Regime II.

method and is defined as the absolute difference normalized by the FEM results, with FEM considered as the ground truth:

$$\frac{|\hat{S}-\hat{S}^*|}{|\hat{S}|}\times 100\%, \qquad \frac{|\hat{U}-\hat{U}^*|}{|\hat{U}|}\times 100\%. \tag{16}$$

Fig. 7(B) provides the same comparison for test Case B ($P = 6.74 \times 10^{-2}$ MPa). The results indicate that, for both test cases, the POD–RBF method predicts stress with relative errors within 0.4% and displacement with relative errors within 0.2%. All computations were performed in the Windows environment on a computer equipped with two AMD EPYC 9454 48-Core Processors. The reported FEM simulation time includes both the Abaqus simulation and the subsequent post-processing/data-extraction procedure used to assemble the snapshot vectors. In Regime I, one FEM simulation requires approximately 30 min; therefore, generating the 17 Regime I training simulations requires approximately 8.5 h of offline FEM computation. After the Regime I FEM database is generated, the POD–RBF training code for Regime I requires 66.02 s on the same computer. Once trained, the POD–RBF model predicts and reconstructs the full-field response for a new pressure input in 0.94 s. The excellent agreement between the POD–RBF predictions and the FEM reference results demonstrates that the hybrid strategy is both accurate and highly efficient for repeated online digital-twin evaluations.

Fig. 8 presents a comparison between the FEM results and POD–RBF predictions for two testing samples from Regime II, where contact occurs. Fig. 8(A) shows the FEM results and POD–RBF-predicted deformations, stress, and displacement fields for test Case C ($P = 3.52 \times 10^{-2}$ MPa, $\Delta H = 35.76$ mm), together with the spatial distribution of relative errors. In this case, the stress prediction errors are below 2%, while the displacement errors are within 0.24%. Because accurately predicting the detailed distribution of contact forces is challenging, we focus instead on the total contact force between the actuator and the rigid plate, which is treated as one separate output parameter. The RBF surrogate is trained to directly predict this total contact force for varying pressures and gap distances. A comparison between the FEM-calculated and RBF-predicted total contact forces is also shown in the figure, with a relative error, defined as the difference between them normalized by the FEM-calculated ground truth, $\left|\hat{F}-\hat{F}^*\right| / \left|\hat{F}\right| \times 100\%$, of 3.42%. Fig. 8(B) presents the same comparison of FEM results and POD–RBF predictions for test Case D from Regime II ($P = 7.05 \times 10^{-2}$ MPa, $\Delta H = 29.74$ mm), including deformations, stress and displacement fields, and total contact force, along with the spatial distribution of their relative errors. In this case, the relative errors in stress and displacement are within 1% and 0.44%, respectively, while the total contact force exhibits a relative error of 2.21%. These results further demonstrate the strong agreement between POD–RBF predictions and FEM reference data, even under the increased nonlinearity introduced by contact. Each FEM simulation in Regime II requires an average computation time of approximately 40 min, including both the Abaqus simulation and the subsequent post-processing/data-extraction procedure; therefore, generating the 85 Regime II training simulations corresponds to approximately 56.7 h of offline FEM computation. After the Regime II FEM database is generated, the POD–RBF training code for Regime II requires 69.47 s on the same computer. Once trained, the surrogate predicts and reconstructs the full-field response for a new pressure-gap-distance input in 0.96 s, highlighting its advantage for real-time digital-twin applications that require repeated evaluations.

Beyond the direct FEM validation shown in Figs. 7 and 8, two additional checks were included to clarify the applicability and necessity of the POD–RBF surrogate. Appendix A examines near-boundary extrapolation outside the sampled training domain, demonstrating that the surrogate should be regarded as a training-bound predictive model rather than an unrestricted extrapolative model. Appendix B compares the POD–RBF predictions with the closest available FEM training samples in the Regime II parameter space. This comparison shows that nearest-sample substitution is insufficient for the contact regime, where small changes in pressure and gap distance can significantly alter the

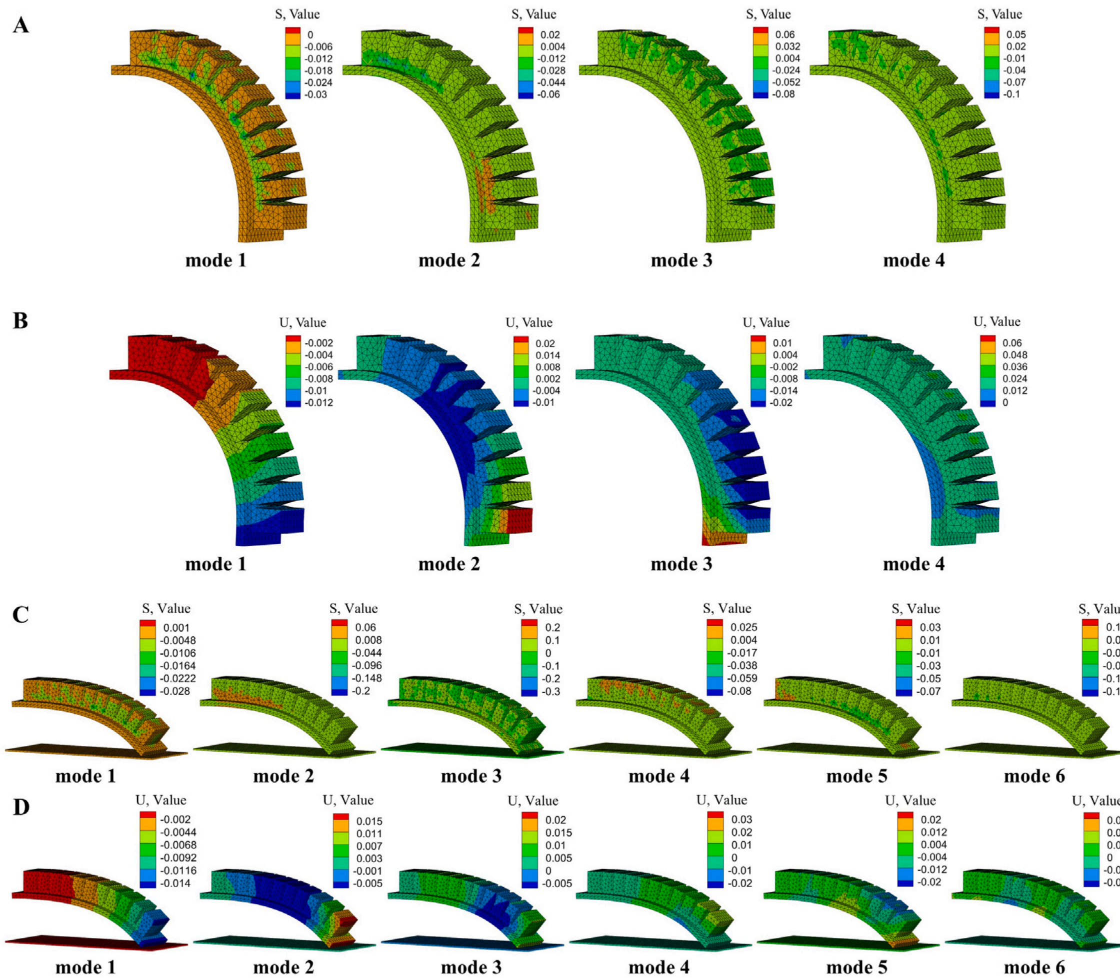

Fig. 6. POD modes used to reconstruct the deformation snapshots of the actuator. The four leading modes for Regime I (non-contact cases) showing (A) stress distribution and (B) displacement distribution projected onto the deformed geometric configuration. The six leading modes for Regime II (contact cases) showing (C) stress distribution and (D) displacement distribution projected onto the deformed geometric configuration.

contact state, contact area, stress localization, and total contact force, thereby necessitating a continuous interpolation strategy.

4.3. Digital twin simulation and demonstration

Having verified the accuracy and efficiency of the POD–RBF hybrid method, this section demonstrates its use for real-time full-field reconstruction of the soft actuator response. Three representative cases are considered: non-contact deformation, transition from non-contact to contact, and initial contact, as summarized in Fig. 9.

Fig. 9(A) shows the experiment and the corresponding digital twin for $\Delta H = 80$ mm. In this case, the actuator bends without contacting the plate throughout the loading process; therefore, the POD–RBF model trained for Regime I is used to construct the digital twin. The actuator is inflated from rest at a flow rate of 125 mL/min until $P = 0.07$ MPa. Real-time pressure readings from a digital pressure gauge are fed into the model, which outputs nodal coordinates, displacement, and stress, with the reconstructed fields visualized in TECPLOT. During the experiment, image snapshots were captured at $P = 0.01$, 0.025, 0.04, 0.055, and 0.07 MPa; the corresponding digital twin deformations, stress, and displacement fields are presented for comparison.

Fig. 9(B) presents the experiment and digital twin for $\Delta H = 40$ mm. In this case, the actuator initially does not contact the plate but bends to make contact as inflation progresses; therefore, both the trained POD–RBF models for Regimes I and II are used to construct the digital twin. The actuator is inflated at 125 mL/min up to $P = 0.07$ MPa. From Fig. 3(H), a critical pressure $P_{C1} = 0.01352$ MPa is identified: for $P \in [0, P_{C1}]$, no contact occurs (Regime I applies); for $P \in (P_{C1}, 0.07\ \text{MPa}]$, contact occurs (Regime II applies). Accordingly, the digital twin switches between the two ROM–surrogate models: Regime I is used for $P \le P_{C1}$ and Regime II for $P > P_{C1}$. The model inputs are the real-time pressure readings, and the outputs—nodal coordinates X, Y, Z, displacement U, stress S, and contact force F—are visualized in TECPLOT. Experimental images at $P = 0.01$, 0.025, 0.04, 0.055, and 0.07 MPa are compared with the corresponding digital twin fields.

Fig. 9(C) presents the experiment and corresponding digital twin prediction for $\Delta H = 15$ mm. In this scenario, the actuator is already in contact with the plate at the initial state due to gravity. The trained POD–RBF model for Regime II is used to construct the digital twin. The actuator is inflated at a rate of 125 mL/min up to $P = 0.07$ MPa. As before, real-time pressure readings serve as inputs to the ROM–surrogate model, while the outputs (X, Y, Z, U, S, F) are visualized in TECPLOT. Snapshots at selected pressure levels are extracted and compared with the corresponding digital twin predictions.

Finally, a soft gripper composed of two actuators is used to demonstrate how the proposed method can support real-time assessment during object grasping. As shown in Fig. 10, both actuators were simultaneously inflated with gas to grasp a cubic block. Because the actuator orientation in the gripper differs from that in the previous single-actuator cases, while gravity remains aligned with the vertical

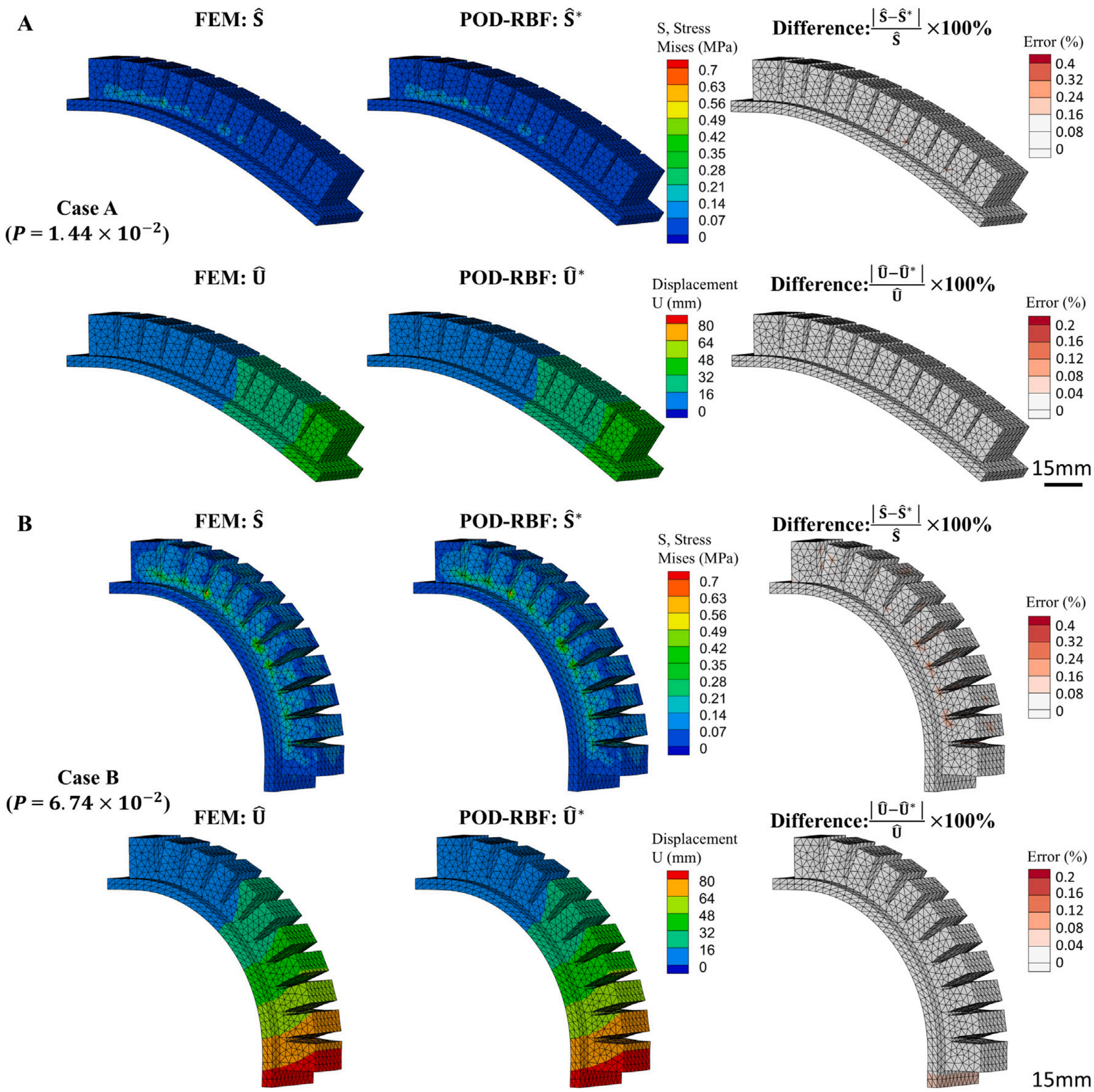

Fig. 7. Comparison of FEM results, POD–RBF predictions, and their differences for two testing samples in Regime I (non-contact cases), showing stress and displacement distributions on the deformed configurations. (A) FEM and POD–RBF predicted deformations, stress, and displacement fields for test Case A (P = 1.44 × 10^{-2} MPa), along with the spatial distribution of the relative error. (B) Same comparison for test Case B (P = 6.74 × 10^{-2} MPa), including the spatial distribution of the relative error.

direction, a separate FEM training database was generated for this configuration. Specifically, 32 FEM training simulations were conducted for the prescribed gap distance of ΔH = 20 mm and used to retrain the surrogate model. The POD–RBF model efficiently reconstructed the deformation, stress distribution, displacement field, and contact force during the grasping process. The digital twin predicted that, at P = 0.079 MPa, each actuator exerted a contact force of 0.58 N on the block. Assuming a typical friction coefficient (f > 0.2), the two contact interfaces provide sufficient frictional resistance to support the weight of the 17 g object. The real-time prediction therefore enables assessment of grasping sufficiency and identification of an appropriate stopping point for inflation. Although this is a simple example, it demonstrates how digital twins can support future real-time control by providing critical information on contact force, deformation, and grasping effectiveness.

This grasping example is intended to demonstrate the POD–RBF training strategy for a prescribed actuator–object configuration, rather than to claim direct prediction for arbitrary objects using the same training data. Interactions with objects of different shapes, contact locations, stiffnesses, or frictional properties would require additional simulations or experiments that include these variables in the input space. The contribution of the present work is therefore the reduced-order surrogate framework itself, in which high-fidelity FEM response fields are compressed by POD and linked to physical input parameters through an RBF surrogate. More complex grasping scenarios could be addressed by enriching the training database with object geometry, compliance, contact position, and sensing information, but such extensions remain future work.

5. Conclusion and future work

SPAs offer intrinsic compliance and safe interaction, making them attractive for soft robotics, biomedical devices, and adaptive mechanical systems. However, their strongly nonlinear material behavior, large deformations, and complex contact interactions pose significant challenges for accurate modeling and real-time prediction. To address this challenge, this work proposed a reduced-order surrogate modeling framework that integrates POD with an RBF surrogate model. The FEM

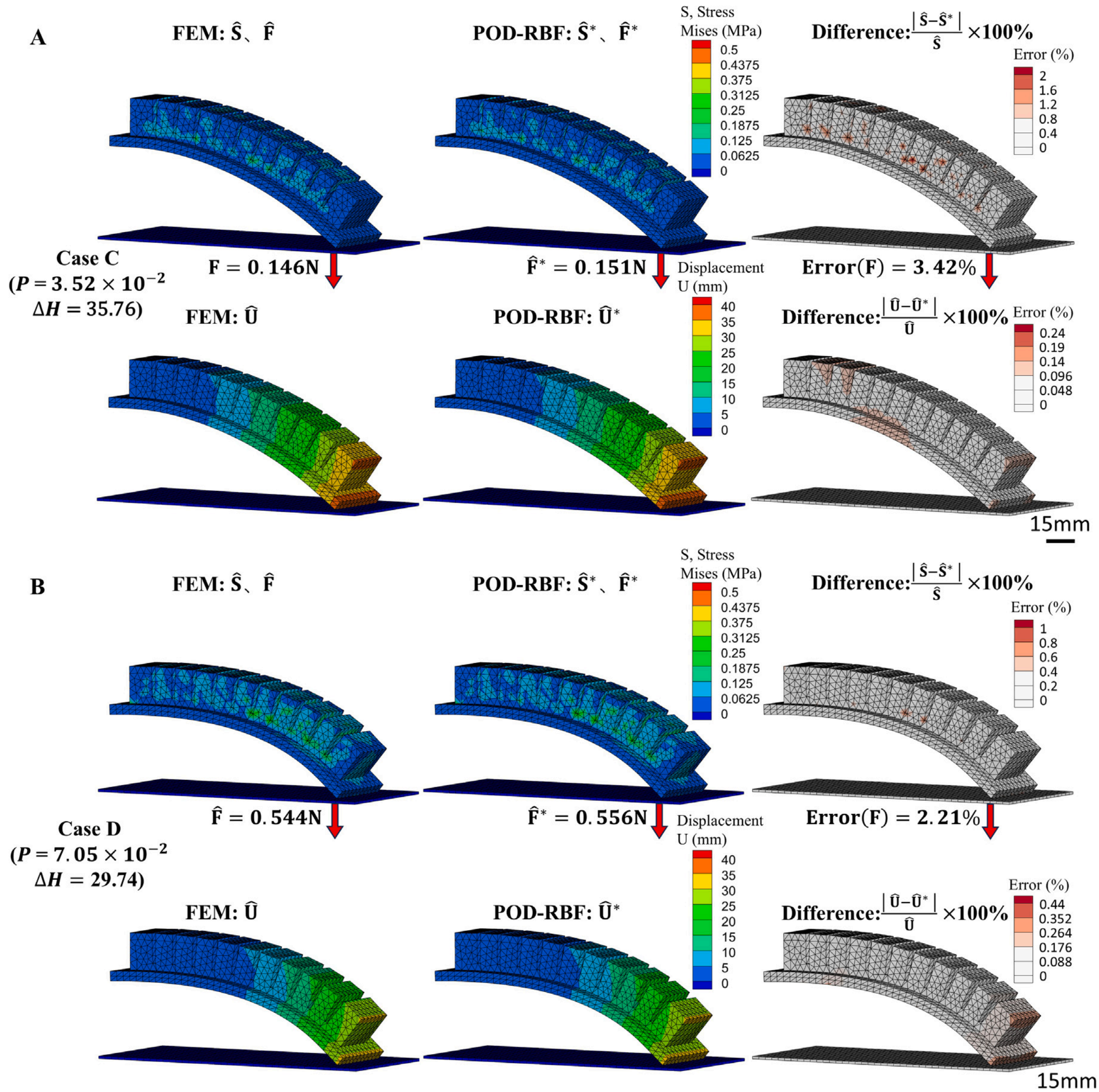

Fig. 8. Comparison of FEM results, POD–RBF predictions, and their differences for two testing samples in Regime II (contact cases), showing stress and displacement distributions on the deformed configurations, along with total contact force. (A) FEM and POD–RBF predicted deformations, stress, and displacement fields for test Case C ($P = 3.52 \times 10^{-2}$ MPa, $\Delta H = 35.76$ mm), including spatial distributions of the relative errors, as well as contact force and associated errors. (B) Same comparison for test Case D ($P = 7.05 \times 10^{-2}$ MPa, $\Delta H = 29.74$ mm), showing FEM and POD–RBF predicted deformations, stress, and displacement fields, the spatial distribution of relative errors, and contact force with errors.

model was first validated against experimental measurements of bending deformation and contact force, providing a reliable high-fidelity database for training. Full-field FEM responses were then projected onto a low-dimensional POD subspace, and the RBF surrogate was trained to map physical inputs to the reduced coordinates. The reconstructed responses were decoded to recover full-field displacement, stress, and contact quantities for new operating conditions.

The proposed framework achieved accurate full-field predictions in both non-contact and contact deformation regimes. For the independent Regime I testing cases, stress and displacement errors remained within 0.4% and 0.2%, respectively. For the independent Regime II testing cases, stress errors were below 2%, displacement errors were within 0.44%, and total contact-force errors were within 3.42%. The offline cost was dominated by generating the FEM training databases, which required approximately 8.5 h for Regime I and 56.7 h for Regime II when Abaqus simulation and post-processing/data extraction were included. Once the databases were generated, POD–RBF training required 66.02 s for Regime I and 69.47 s for Regime II. The trained surrogate then required only 0.94 s and 0.96 s for online prediction and full-field reconstruction in Regime I and Regime II, respectively, compared with approximately 30–40 min for one high-fidelity FEM simulation. The method was further demonstrated on a two-actuator soft gripper, showing its potential for real-time assessment of deformation, contact force, and grasping sufficiency.

The present framework should be interpreted within its sampled and experimentally validated operating envelope. It provides an interpolative surrogate of high-fidelity FEM simulations rather than an unrestricted extrapolative predictor for arbitrary unseen environments. Additional results show that the model is most reliable for accurate prediction within the sampled domain, without extrapolation, and

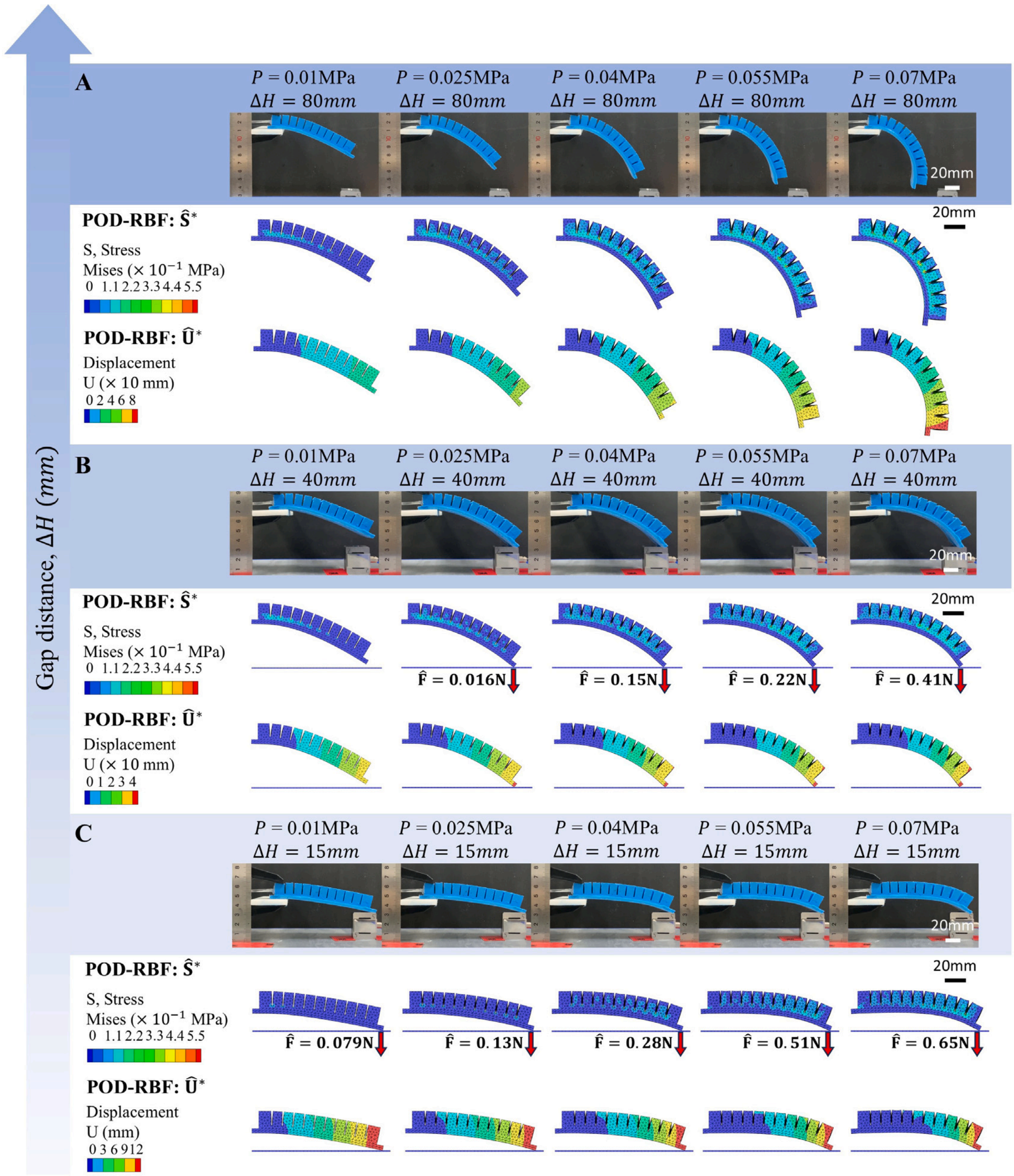

Fig. 9. Digital-twin demonstrations of the SPA under three representative gap distances. The vertical gradient arrow indicates the decrease in gap distance ΔH from 80 mm to 15 mm. The actuator is inflated from rest at a flow rate of 125 mL/min until the pressure reaches $P = 0.07$ MPa. Experimental snapshots and POD–RBF-predicted full-field stress and displacement distributions are shown at selected pressure levels of $P = 0.01$, 0.025, 0.04, 0.055, and 0.07 MPa. (A) Digital-twin prediction for $\Delta H = 80$ mm, where the actuator bends without contacting the plate throughout the loading process. (B) Digital-twin prediction for $\Delta H = 40$ mm, where the actuator initially does not contact the plate but transitions into contact as inflation progresses. (C) Digital-twin prediction for $\Delta H = 15$ mm, where the actuator is already in contact with the plate at the initial state due to gravity. For the contact cases, the predicted total contact force is also shown.

that a continuous POD–RBF surrogate is necessary because nearest-sample replacement cannot adequately capture contact-driven changes in deformation, stress localization, and contact force. Accordingly, this work should be viewed as a stepping stone toward a true soft-robot digital twin with predictive capacity beyond the training bounds. Several directions remain for future work. The current snapshot matrix construction assumes a fixed nodal topology, which limits direct treatment of geometric variations such as changes in actuator length, width, or height. Background grid methods and inverse distance weighting, which enforce a consistent computational grid across varying geometries, offer a promising route to incorporate geometric parametrization within POD-based frameworks (Yang et al., 2024). Reliable prediction outside the training domain will also require additional developments, such as physics-informed constraints, adaptive sampling, and uncertainty-aware surrogate models. In addition, integrating multi-sensor feedback, sensor fusion, and online model updating would improve prediction accuracy and robustness under unseen loading, contact, or environmental conditions, while coupling the digital twin with active control strategies could support autonomous and adaptive manipulation.

In summary, the POD–RBF hybrid strategy provides an efficient framework for constructing FEM-based digital twins of SPAs. By achieving near-real-time prediction while preserving high-fidelity full-field mechanical information, the proposed approach offers a practical route

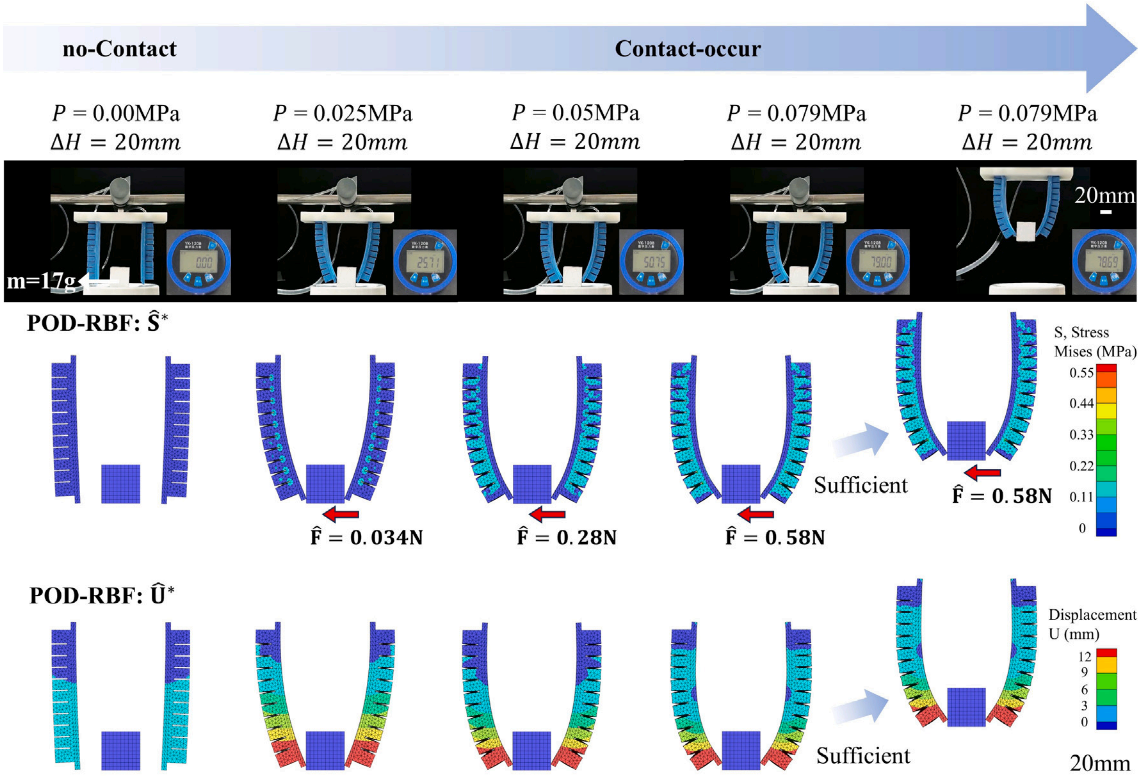

Fig. 10. Experimental setup and corresponding digital twin prediction for a soft robotic gripper composed of two actuators grasping an object at a gap distance of $\Delta H = 20$ mm.

toward digital twins for soft robotic systems. Addressing the remaining challenges related to geometric parametrization, extrapolation capability, and sensor integration will further improve the scalability and reliability of this framework for real-time and safety–critical applications.

CRediT authorship contribution statement

Yichen Pu: Writing – review & editing, Writing – original draft, Validation, Methodology, Investigation. **Xinjie Hu:** Validation. **Xingrui Liu:** Validation. **Shichao Niu:** Funding acquisition, Conceptualization. **Ning An:** Writing – review & editing, Writing – original draft, Supervision, Project administration, Conceptualization.

Declaration of competing interest

The authors declare that they have no known competing financial interests or personal relationships that could have appeared to influence the work reported in this paper.

Acknowledgments

This research is supported by the National Natural Science Foundation of China (grant 12202295), International (Regional) Cooperation and Exchange Projects of the National Natural Science Foundation of China (grant W2421002), Sichuan Science and Technology Program (grant 2025ZNSFSC0845), and the Opening Project of the Key Laboratory of Bionic Engineering (Ministry of Education), Jilin University (No. K202403). Ning An also acknowledges support from the China Scholarship Council (No. 202506240177).

Appendix A. Near-boundary extrapolation outside the sampled domain

This appendix examines the predictive behavior of the POD–RBF surrogate for input parameters located outside the sampled training domain. The objective is not to establish unrestricted extrapolation capability, but to quantify the practical operating boundary of the present data-driven digital twin. This assessment is relevant because digital-twin queries may occur near the limits of the prescribed operating envelope. Since the actuator response is separated into two mechanically distinct regimes, the extrapolation assessment was conducted separately for Regime I, where no contact occurs and pressure P is the only input, and Regime II, where contact occurs and both pressure P and gap distance ΔH are inputs.

For Regime I, the surrogate was trained over $0 \le P \le 0.09$ MPa. To assess near-boundary extrapolation, two pressures outside this range were considered: $P = 9.2 \times 10^{-2}$ MPa and $P = 0.1$ MPa, denoted as Cases E and F, respectively. As shown in Fig. A.11, the POD–RBF model reproduces the overall deformation pattern and displacement field for Case E, which is only slightly outside the training range. The maximum plotted relative errors for this case are approximately 28.5% in stress and 4.4% in displacement. For the farther out-of-domain Case F, the maximum plotted errors increase to approximately 42.9% and 15.0%, respectively, with the largest discrepancies localized near stress concentrations around the chamber walls. These errors are substantially larger than those obtained for the independent Regime I testing cases within the sampled domain in Fig. 7, where the stress and displacement errors remain within 0.4% and 0.2%, respectively.

For Regime II, the surrogate was trained over $0 \le P \le 0.09$ MPa and $10 \le \Delta H \le 50$ mm. To assess extrapolation in the two-dimensional contact regime, two out-of-domain cases were considered: Case G with $P = 9.2 \times 10^{-2}$ MPa and $\Delta H = 8$ mm, and Case H with $P = 0.1$ MPa

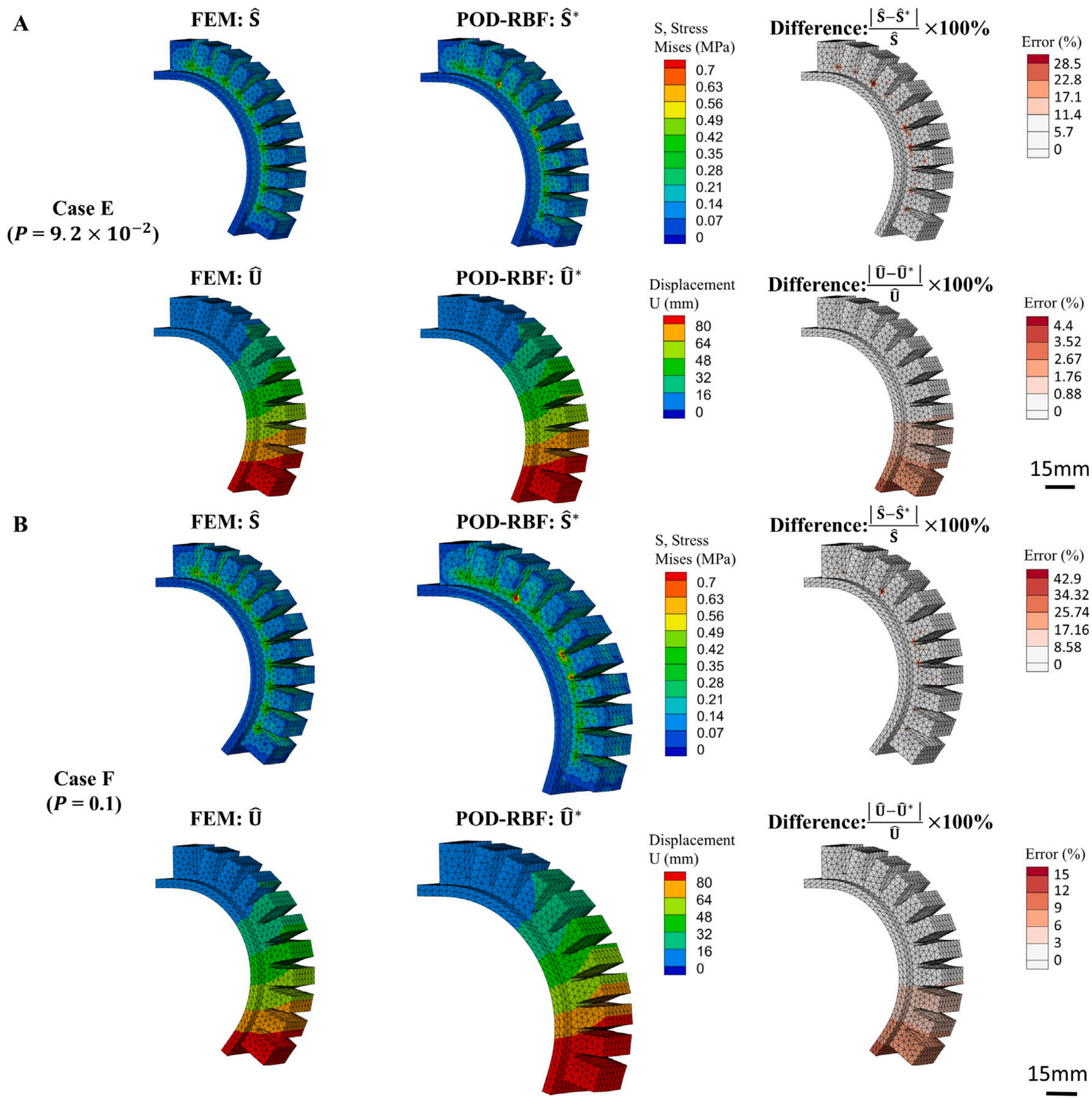

Fig. A.11. Extrapolation assessment of the POD–RBF model for Regime I (non-contact cases). The model was trained within $0 \le P \le 0.09$ MPa and tested at two pressures outside this range: (A) Case E, $P = 9.2 \times 10^{-2}$ MPa, and (B) Case F, $P = 0.1$ MPa. FEM-calculated stress and displacement fields are compared with the POD–RBF predictions, and the spatial distributions of relative errors are shown. The results indicate that near-boundary extrapolation preserves the overall deformation pattern, while local stress and displacement errors increase as the pressure moves farther outside the training range.

and $\Delta H = 55$ mm. As shown in Fig. A.12, Case G is outside but close to the sampled domain and retains reasonable agreement for the total contact force, with a relative force error of 2.28% (0.942 N predicted by POD–RBF versus 0.964 N calculated by FEM). However, the maximum plotted field errors reach approximately 30% for stress and 15% for displacement. For the farther out-of-domain Case H, the contact-force error increases to 14.23% (0.741 N predicted by POD–RBF versus 0.864 N calculated by FEM), while the maximum plotted stress and displacement errors reach approximately 40% and 20%, respectively. These errors are substantially larger than those obtained for the independent Regime II testing cases in Fig. 8, where the stress errors are below 2%, the displacement errors are within 0.44%, and the total contact-force errors are within 3.42%.

Together, these quantitative comparisons demonstrate that extrapolation produces substantially larger errors than interpolation within the validated training domain. The POD–RBF surrogate can retain useful predictive accuracy for out-of-domain inputs close to the sampled boundary, but should be regarded as a training-bound predictive model rather than an unrestricted extrapolative model. This limitation is particularly evident in the contact regime, where changes in pressure and gap distance can alter the contact area, contact force, stress localization, and overall deformation state.

Appendix B. Nearest-sample replacement within the sampled domain

This appendix evaluates whether the desired actuator response can be approximated by simply selecting the closest available FEM training sample. This nearest-sample baseline provides a direct test of whether the interpolation task addressed in this work is merely a lookup problem over a discrete simulation database, or whether a continuous reduced-order surrogate is needed. The analysis is performed for Regime II because contact introduces stronger nonlinearity, and small changes in pressure P or gap distance ΔH can modify the contact state, stress localization, deformation field, and total contact force.

The Regime II surrogate was trained over $0 \le P \le 0.09$ MPa and $10 \le \Delta H \le 50$ mm. In the present model, each input corresponds

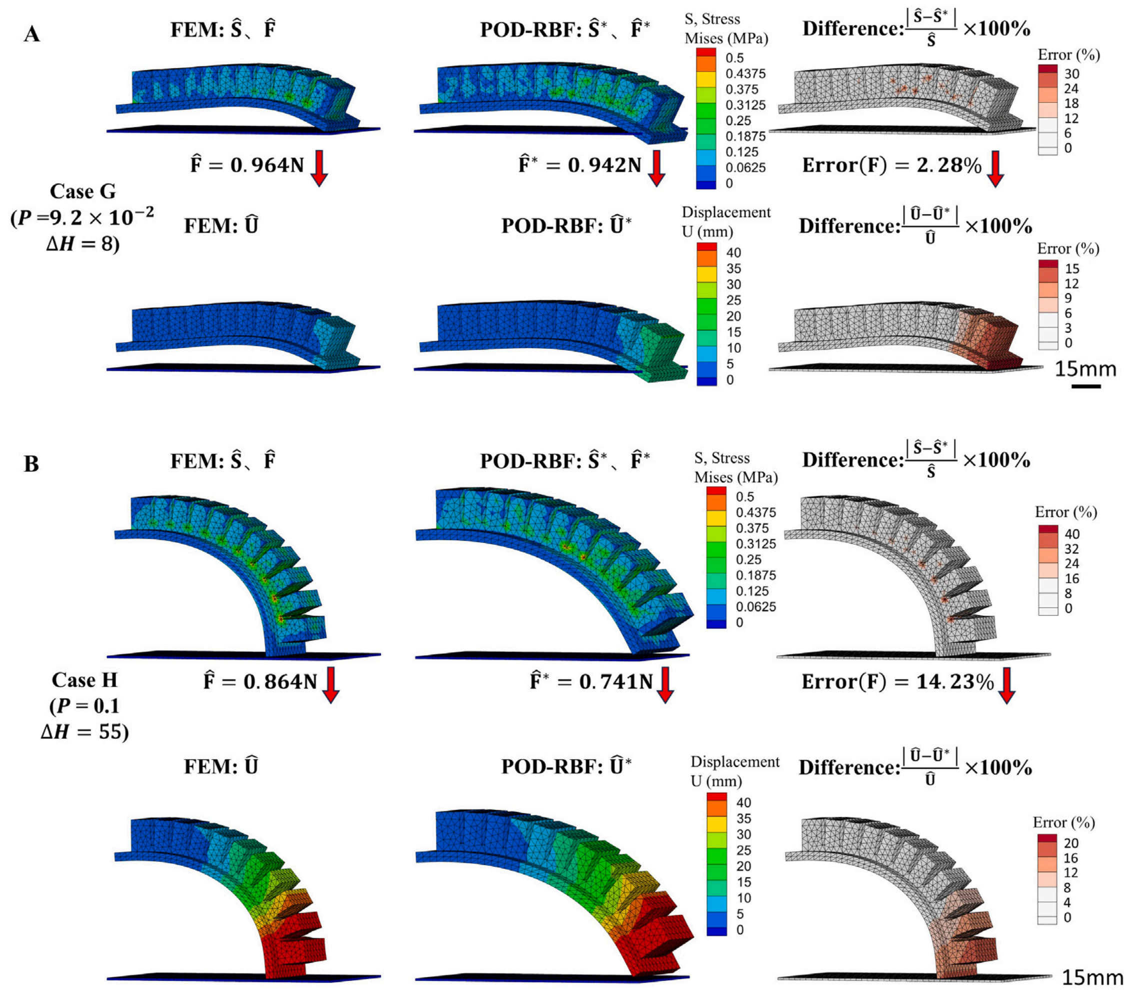

Fig. A.12. Extrapolation assessment of the POD–RBF model for Regime II (contact cases). The model was trained within $0 \leq P \leq 0.09$ MPa and $10 \leq \Delta H \leq 50$ mm, and tested at two parameter sets outside this domain: (A) Case G, $P = 9.2 \times 10^{-2}$ MPa and $\Delta H = 8$ mm, and (B) Case H, $P = 0.1$ MPa and $\Delta H = 55$ mm. FEM-calculated stress, displacement, and total contact force are compared with the POD–RBF predictions. The relative error in total contact force is 2.28% for Case G and 14.23% for Case H, showing that the model remains useful close to the training boundary but becomes less reliable when extrapolating farther outside the pressure–gap-distance domain.

to a full-field FEM snapshot with 125,110 entries; nearest-sample replacement therefore substitutes an entire discrete FEM state rather than interpolating the reduced coordinates.

The selected target cases and their closest training samples are shown in Fig. B.13, and the corresponding field comparisons are shown in Fig. B.14. For the first comparison, the target case is $P = 3.52 \times 10^{-2}$ MPa and $\Delta H = 35.76$ mm, while the closest sample is $P = 3.23 \times 10^{-2}$ MPa and $\Delta H = 38.58$ mm. Nearest-sample replacement gives a relative total-contact-force error of 22.6% (0.113 N versus 0.146 N), whereas the POD–RBF prediction error is 3.42% (Fig. 8(A)). The maximum plotted stress and displacement differences caused by nearest-sample replacement are approximately 2% and 8%, respectively, compared with POD–RBF stress and displacement errors below 2% and within 0.24%, respectively.

For the second comparison, the target case is $P = 7.05 \times 10^{-2}$ MPa and $\Delta H = 29.74$ mm, while the closest sample is $P = 7.82 \times 10^{-2}$ MPa and $\Delta H = 31.44$ mm. Nearest-sample replacement gives a contact-force error of 15.4% (0.628 N versus 0.544 N), whereas the POD–RBF prediction error is 2.21% (Fig. 8(B)). The corresponding maximum plotted stress and displacement differences are approximately 5% and 7.5%, respectively, compared with POD–RBF errors within 1% and 0.44%, respectively.

These comparisons show that nearest-sample replacement is insufficient even when neighboring points appear close in parameter space. In

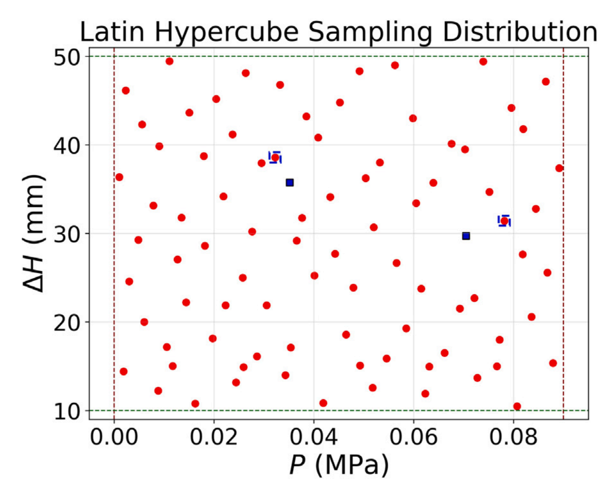

Fig. B.13. Distribution of the Latin hypercube samples in the Regime II parameter space. Red circles denote the training samples within the pressure-gap-distance domain. The blue markers denote two target test cases and their corresponding closest training samples, which are used to evaluate whether nearest-sample replacement can approximate the target full-field FEM response.

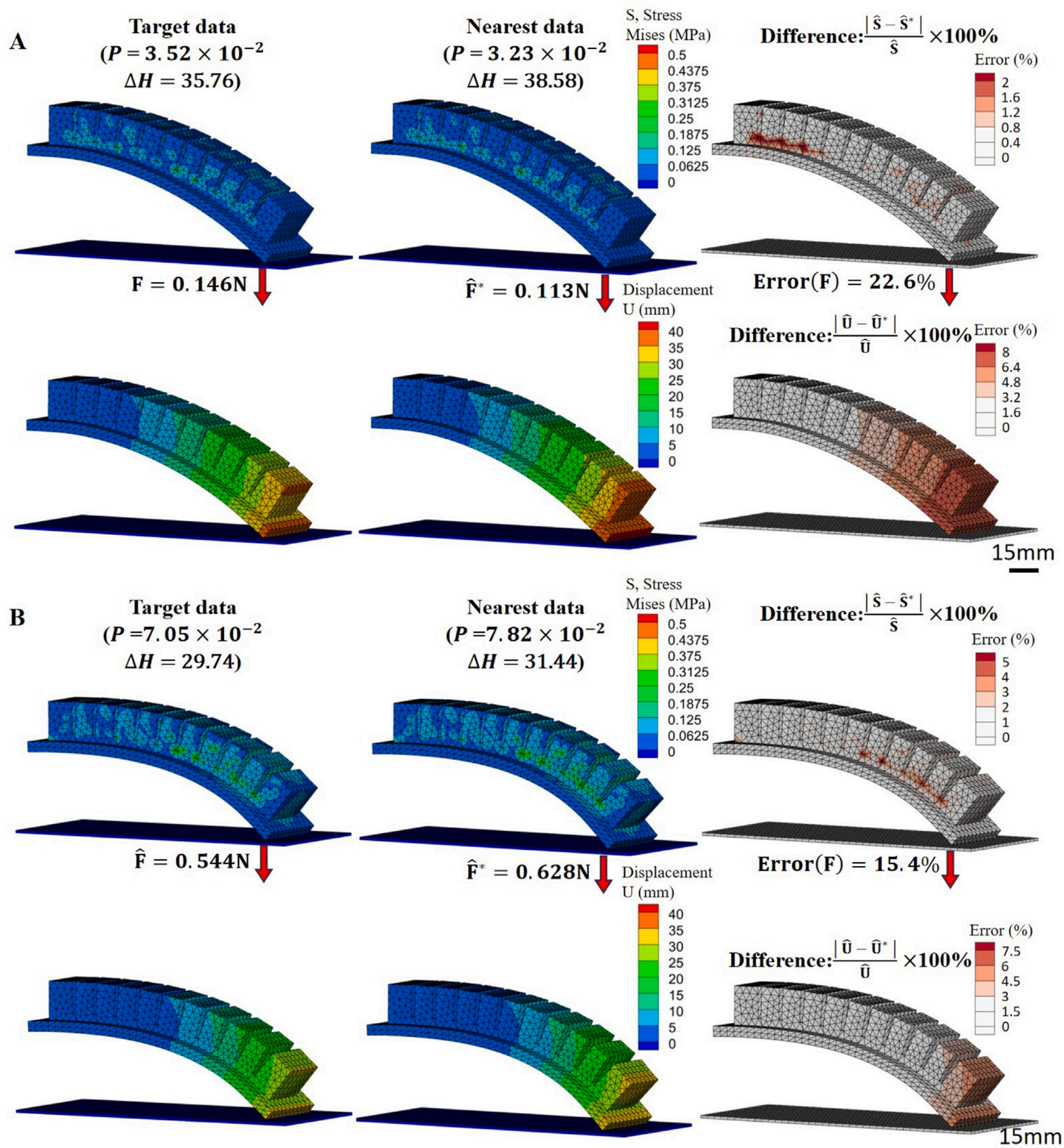

Fig. B.14. Comparison between the target test cases and their closest training samples in Regime II. (A) Target case with $P = 3.52\times10^{-2}$ MPa and $\Delta H = 35.76$ mm, compared with the closest training sample with $P = 3.23\times10^{-2}$ MPa and $\Delta H = 38.58$ mm. (B) Target case with $P = 7.05\times10^{-2}$ MPa and $\Delta H = 29.74$ mm, compared with the closest training sample with $P = 7.82\times10^{-2}$ MPa and $\Delta H = 31.44$ mm. The differences in stress, displacement, and contact force show that selecting a nearby discrete simulation cannot replace a continuous reduced-order surrogate for full-field digital-twin prediction.

Regime II, small changes in P and ΔH can alter the contact state, contact area, deformation field, stress distribution, and total contact force. The POD–RBF framework avoids this piecewise-constant approximation by constructing a continuous reduced-order mapping for full-field FEM reconstruction.

Data availability

The source code for reproducing the digital twin simulations works presented in the paper can be downloaded from https://github.com/SCU-An-Group/DT4SoRo.

References

An, N., Li, M., Zhou, J., 2018. Modeling and understanding locomotion of pneumatic soft robots. Soft Mater. 16 (3), 151–159.

Aversano, G., Bellemans, A., Li, Z., Coussement, A., Gicquel, O., Parente, A., 2019. Application of reduced-order models based on PCA & Kriging for the development of digital twins of reacting flow applications. Comput. Chem. Eng. 121, 422–441.

Ayoub, N., Deü, J.-F., Larbi, W., Pais, J., Rouleau, L., 2022. Application of the POD method to nonlinear dynamic analysis of reinforced concrete frame structures subjected to earthquakes. Eng. Struct. 270, 114854.

Chen, Z., Renda, F., Le Gall, A., Mocellin, L., Bernabei, M., Dangel, T., Ciuti, G., Cianchetti, M., Stefanini, C., 2024. Data-driven methods applied to soft robot modeling and control: A review. IEEE Trans. Autom. Sci. Eng. 22, 2241–2256.

Chen, Q., Yuan, C., Wang, T., 2026. Machine learning-energized framework for rapid and precise inverse design of programmable structures with multiple design variables. J. Mech. Phys. Solids 106524.

Ferrentino, P., Lopez-Diaz, A., Terryn, S., Legrand, J., Brancart, J., Van Assche, G., Vazquez, E., Vazquez, A., Vanderborght, B., 2022. Quasi-static FEA model for a multi-material soft pneumatic actuator in SOFA. IEEE Robot. Autom. Lett. 7 (3), 7391–7398.

Gent, A.N., 1996. A new constitutive relation for rubber. Rubber Chem. Technol. 69 (1), 59–61.

Gorissen, B., Melancon, D., Vasios, N., Torbati, M., Bertoldi, K., 2020. Inflatable soft jumper inspired by shell snapping. Sci. Robot. 5 (42), eabb1967.

Goury, O., Carrez, B., Duriez, C., 2021. Real-time simulation for control of soft robots with self-collisions using model order reduction for contact forces. IEEE Robot. Autom. Lett. 6 (2), 3752–3759.

Goury, O., Duriez, C., 2018. Fast, generic, and reliable control and simulation of soft robots using model order reduction. IEEE Trans. Robot. 34 (6), 1565–1576.

Gu, G., Wang, D., Ge, L., Zhu, X., 2021. Analytical modeling and design of generalized pneu-net soft actuators with three-dimensional deformations. Soft Robot. 8 (4), 462–477.

He, X., Yang, L., Gong, Z., Pang, Y., Li, J., Kan, Z., Song, X., 2025. Digital twin-based online structural optimization? Yes, it's possible! Thin-Walled Struct. 208, 112796.

Ilievski, F., Mazzeo, A.D., Shepherd, R.F., Chen, X., Whitesides, G., 2011. Soft robotics for chemists.

Jin, T., Sun, Z., Li, L., Zhang, Q., Zhu, M., Zhang, Z., Yuan, G., Chen, T., Tian, Y., Hou, X., et al., 2020. Triboelectric nanogenerator sensors for soft robotics aiming at digital twin applications. Nat. Commun. 11 (1), 5381.

Lai, X., Yang, L., He, X., Pang, Y., Song, X., Sun, W., 2023. Digital twin-based structural health monitoring by combining measurement and computational data: An aircraft wing example. J. Manuf. Syst. 69, 76–90.

Li, Y., Liu, W., Zhang, Y., Zhang, W., Gao, C., Chen, Q., Ji, Y., 2023. Interactive real-time monitoring and information traceability for complex aircraft assembly field based on digital twin. IEEE Trans. Ind. Inform. 19 (9), 9745–9756.

Liberge, E., Hamdouni, A., 2010. Reduced order modelling method via proper orthogonal decomposition (POD) for flow around an oscillating cylinder. J. Fluids Struct. 26 (2), 292–311.

Liu, M., Fang, S., Dong, H., Xu, C., 2021. Review of digital twin about concepts, technologies, and industrial applications. J. Manuf. Syst. 58, 346–361.

Liu, J., Low, J.H., Han, Q.Q., Lim, M., Lu, D., Yeow, C.-H., Liu, Z., 2022. Simulation data driven design optimization for reconfigurable soft gripper system. IEEE Robot. Autom. Lett. 7 (2), 5803–5810.

Lu, Y., Hu, X., Pu, Y., Yu, Z., An, N., Tang, S., Guo, X., 2026. A LLM-inspired experimental-data-driven framework for viscoelastic soft structures. Int. J. Mech. Sci. 111696.

Mengaldo, G., Renda, F., Brunton, S.L., Bächer, M., Calisti, M., Duriez, C., Chirikjian, G.S., Laschi, C., 2022. A concise guide to modelling the physics of embodied intelligence in soft robotics. Nat. Rev. Phys. 4 (9), 595–610.

Mosadegh, B., Polygerinos, P., Keplinger, C., Wennstedt, S., Shepherd, R.F., Gupta, U., Shim, J., Bertoldi, K., Walsh, C.J., Whitesides, G.M., 2014. Pneumatic networks for soft robotics that actuate rapidly. Adv. Funct. Mater. 24 (15), 2163–2170.

Moseley, P., Florez, J.M., Sonar, H.A., Agarwal, G., Curtin, W., Paik, J., 2016. Modeling, design, and development of soft pneumatic actuators with finite element method. Adv. Eng. Mater. 18 (6), 978–988.

Muller, N., Magaia, L., Herbst, B.M., 2004. Singular value decomposition, eigenfaces, and 3D reconstructions. SIAM Rev. 46 (3), 518–545.

Polygerinos, P., Wang, Z., Overvelde, J.T., Galloway, K.C., Wood, R.J., Bertoldi, K., Walsh, C.J., 2015. Modeling of soft fiber-reinforced bending actuators. IEEE Trans. Robot. 31 (3), 778–789.

Pu, Y., Zheng, S., Hu, X., Tang, S., An, N., 2024. Robotic skins inspired by auxetic metamaterials for programmable bending of soft actuators. Mater. Des. 246, 113334.

Schegg, P., Ménager, E., Khairallah, E., Marchal, D., Dequidt, J., Preux, P., Duriez, C., 2023. SofaGym: An open platform for reinforcement learning based on soft robot simulations. Soft Robot. 10 (2), 410–430.

Shepherd, R.F., Ilievski, F., Choi, W., Morin, S.A., Stokes, A.A., Mazzeo, A.D., Chen, X., Wang, M., Whitesides, G.M., 2011. Multigait soft robot. Proc. Natl. Acad. Sci. 108 (51), 20400–20403.

Taira, K., Hemati, M.S., Brunton, S.L., Sun, Y., Duraisamy, K., Bagheri, S., Dawson, S.T., Yeh, C.-A., 2020. Modal analysis of fluid flows: Applications and outlook. AIAA J. 58 (3), 998–1022.

Tao, F., Qi, Q., 2019. Make more digital twins. Nature 573 (7775), 490–491.

Tao, F., Xiao, B., Qi, Q., Cheng, J., Ji, P., 2022. Digital twin modeling. J. Manuf. Syst. 64, 372–389.

Wang, Z., Polygerinos, P., Overvelde, J.T., Galloway, K.C., Bertoldi, K., Walsh, C.J., 2016. Interaction forces of soft fiber reinforced bending actuators. IEEE/ASME Trans. Mechatronics 22 (2), 717–727.

Wang, J., Wang, D., Dong, L., Zhang, M., Gu, G., 2023. Analytical modeling and inverse design of centimeter-scale hard-magnetic soft robots. IEEE Trans. Autom. Sci. Eng.

Wang, X., Wang, B., Pinskier, J., Xie, Y., Brett, J., Scalzo, R., Howard, D., 2024. Fin-bayes: A multi-objective Bayesian optimization framework for soft robotic fingers. Soft Robot. 11 (5), 791–801.

Wang, Y., Yu, B., Cao, Z., Zou, W., Yu, G., 2012. A comparative study of POD interpolation and POD projection methods for fast and accurate prediction of heat transfer problems. Int. J. Heat Mass Transfer 55 (17–18), 4827–4836.

Xavier, M.S., Fleming, A.J., Yong, Y.K., 2021. Finite element modeling of soft fluidic actuators: Overview and recent developments. Adv. Intell. Syst. 3 (2), 2000187.

Xavier, M.S., Tawk, C.D., Fleming, A., Zolfagharian, A., Pinskier, J., Howard, D., Young, T., Lai, J., Harrison, S.M., Yong, Y.K., et al., 2022. Soft pneumatic actuators: A review of design, fabrication, modeling, sensing, control and applications.

Xiao, W., Xie, C., Xiao, Y., Tang, K., Wang, Z., Hu, D., Ding, R., Jiao, Z., 2025. A new vacuum-powered soft bending actuator with programmable variable curvatures. Mater. Des. 250, 113641.

Xie, Z., Domel, A.G., An, N., Green, C., Gong, Z., Wang, T., Knubben, E.M., Weaver, J.C., Bertoldi, K., Wen, L., 2020. Octopus arm-inspired tapered soft actuators with suckers for improved grasping. Soft Robot. 7 (5), 639–648.

Yang, Y., Zhao, X., Cheng, Q., Guo, R., Li, M., Zhou, J., 2024. POD–ANN as digital twins for surge line thermal stratification. Nucl. Eng. Des. 428, 113487.

Zhang, Z., Jin, Z., Gu, G.X., 2022. Efficient pneumatic actuation modeling using hybrid physics-based and data-driven framework. Cell Rep. Phys. Sci. 3 (4).

Zhong, G., Dou, W., Zhang, X., Yi, H., 2021. Bending analysis and contact force modeling of soft pneumatic actuators with pleated structures. Int. J. Mech. Sci. 193, 106150.

Zou, S., Picella, S., De Vries, J., Kortman, V.G., Sakes, A., Overvelde, J.T., 2024. A retrofit sensing strategy for soft fluidic robots. Nat. Commun. 15 (1), 539.